SPH simulations of star formation triggered by expanding HII regions

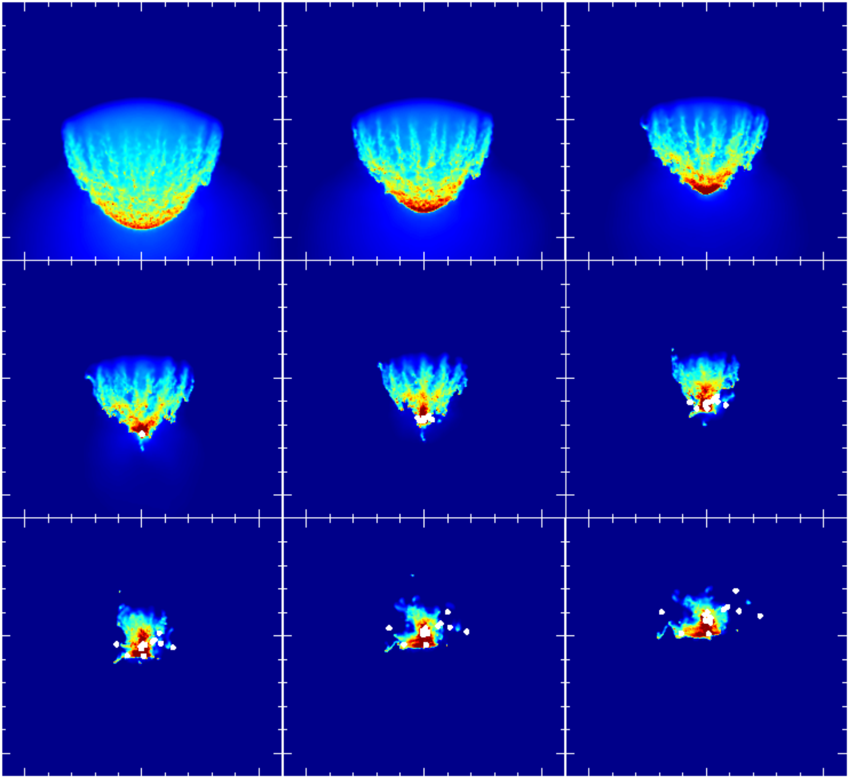

Thomas G. Bisbas
Cardiff University

llaborators: Anthony Whitworth, Richard Wünsch, David Hubber and Stefanie Wa

Prague, 16th September 2009. CONSTELLATION meeting.

Outline

1. Radiation Driven Compression
2. Numerical treatment and transport of ionizing photons
3. Description of the simulations
4. Results
5. Conclusions

Radiation Driven Compression

Radiation Driven Compression

The structure of the interstellar medium is observed to be extremely irregular and to contain many clouds.

As an HII region expands, it may overrun and compress pre-existing nearby clouds, causing them to collapse.

As they collapse, their internal thermal pressure increases and this leads to re-expansion.

After re-expansion, a cometary tail is formed extending away from the ionizing source.

The above process is known as *Radiation Driven Compression* (or Implosion).

Lefloch & Lazareff (1994)

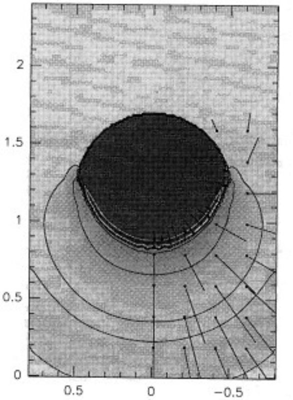

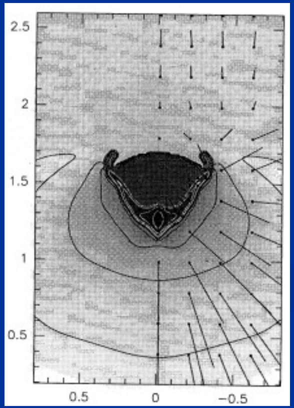

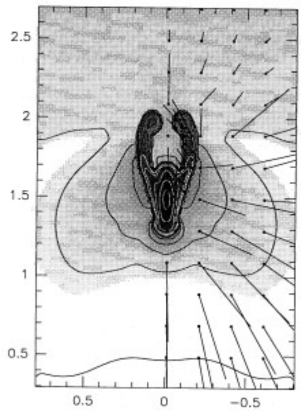

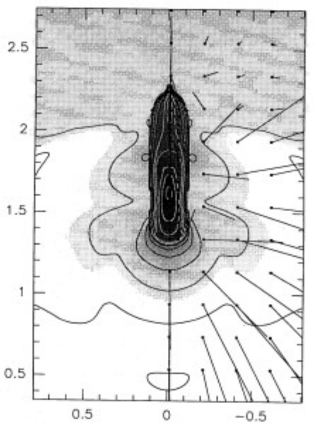

Radiation Driven Compression

If the head of this cometary structure is too dense, it fragments. These globules are therefore potential sites of star formation.

Various observations show the existence of these structures (*Sugitani et al. 1999; Lefloch & Lazareff 1995; Lefloch et al. 1997; Morgan et al. 2008; and others*).

Several workers have tried to simulate the Radiation Driven Compression process.

Some of these simulations concentrate on the morphology of the resulting bright-rimmed clouds (*Sandford et al. 1982; Bertoldi 1989; Lefloch & Lazareff 1994; Miao et al. 2006; Henney et al. 2008*), and some others explore the possibility that the collapse of a bright-rimmed cloud might sometimes lead to triggered star formation (*Kessel-Deynet & Burkert 2003; Dale et al. 2005; Miao et al. 2008; Gritschneder et al. 2009*).

However, as *Deharveng et al. (2005)* mention, “no model explains *where* star formation takes place (in the core or at its periphery) or *when* (during the maximum compression phase, or earlier).”

Numerical treatment and transport of ionizing photons

Numerical treatment and transport of ionizing photons

The *D* – type expansion of an HII region

The ionization front (IF) is located where

$$\int_{r'=0}^{r'=R_{\mathrm{IF}}} \rho^2(r') r'^2 dr' = \frac{m^2 \dot{N}_{\mathrm{LyC}}}{4\pi\alpha_{\mathrm{B}}} \equiv I_{\max}$$

where $m = m_p / X$.
In the simulations presented here we use $X=0.7$ which corresponds to H_2

The integral which we want to solve is:

$$I(r) = \int_{r'=0}^{r'=r} \rho^2(r') r'^2 dr'$$

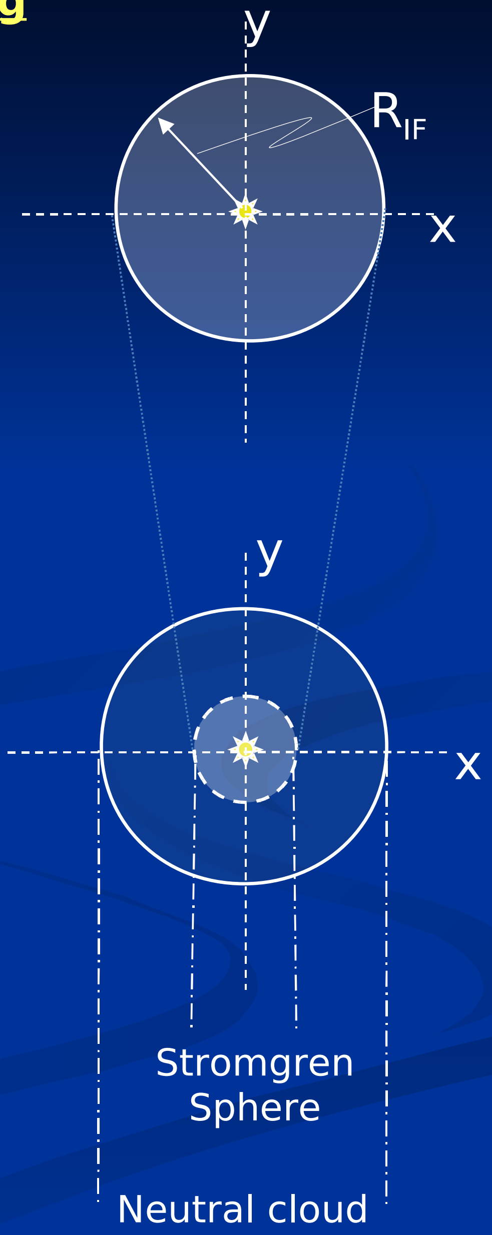
y
R_{IF}
x
y
x
Stromgren Sphere
Neutral cloud

Numerical treatment and transport of ionizing photons

Ray Casting

We use SEREN SPH code (*Hubber et al. 2009, in preparation*).

We use HEALPix algorithm (*Gorski et al. 2005*) to generate a uniform set of rays, in order to determine the overall shape of the ionization front.

How many rays? $N_\ell = 12 \times 4^\ell$ where ℓ is the level of refinement

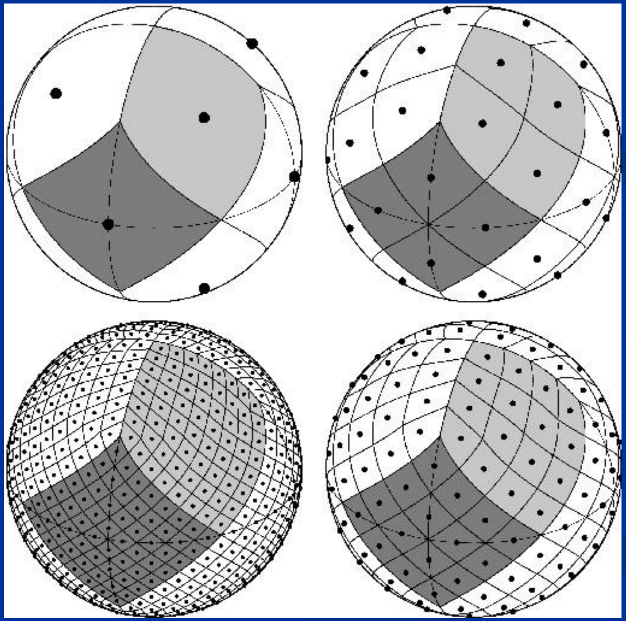

Gorski et al. (1999)

Numerical treatment and transport of ionizing photons

Ray Casting

To perform the integration we define a set of discrete evaluation points. The SPH density at each point is

$$\rho_j = \sum_k \left\{ \frac{m_k}{h_j^3} W\left(\frac{|\mathbf{r}_k - \mathbf{r}_j|}{h_j} \right) \right\}$$

We use the trapezium method of integration to calculate the integral *I*.

$$\begin{aligned} I(r_j) &= \int_{r=0}^{r=r_j} \rho^2 (r\hat{\mathbf{e}})\, r^2 \,\mathrm{d}r \\ &\simeq \sum_{j'=1}^{j'=j} \left\{ \left(\frac{\rho_{j'-1}^2 r_{j'-1}^2 + \rho_{j'}^2 r_{j'}^2}{2} \right) f_1 h_{j'-1} \right\} \end{aligned}$$

The next evaluation point is

$$\mathbf{r}_{j'+1} = \mathbf{r}_{j'} + f_1 h_{j'} \hat{\mathbf{e}}$$

Acceptable accuracy is obtained with f_1=0.25

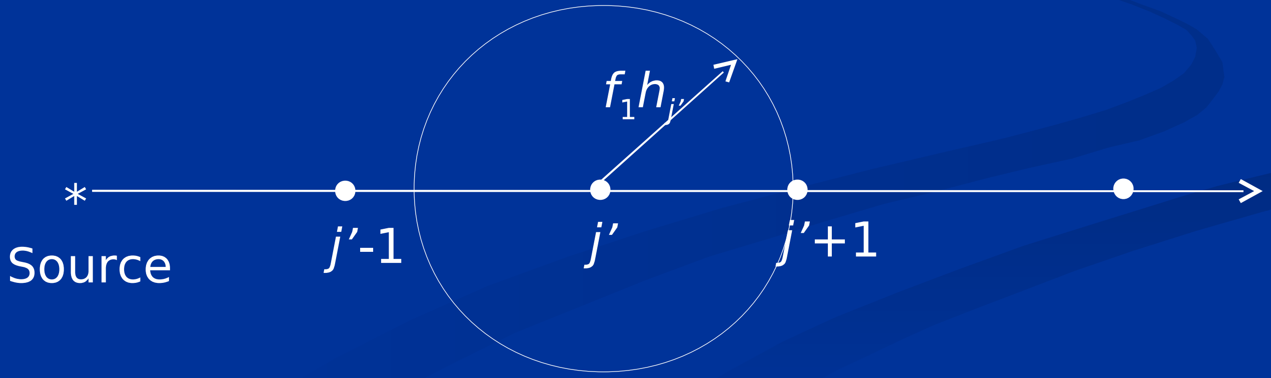

Numerical treatment and transport of ionizing photons

Ray Splitting

A ray is split into four child-rays as soon as its linear separation from the neighbouring rays exceeds $f_2 h_j$

$$\ell \geq \log_2\left(\frac{r_j}{f_2 h_j}\right)$$

Acceptable accuracy is obtained with $f_2=0.5$

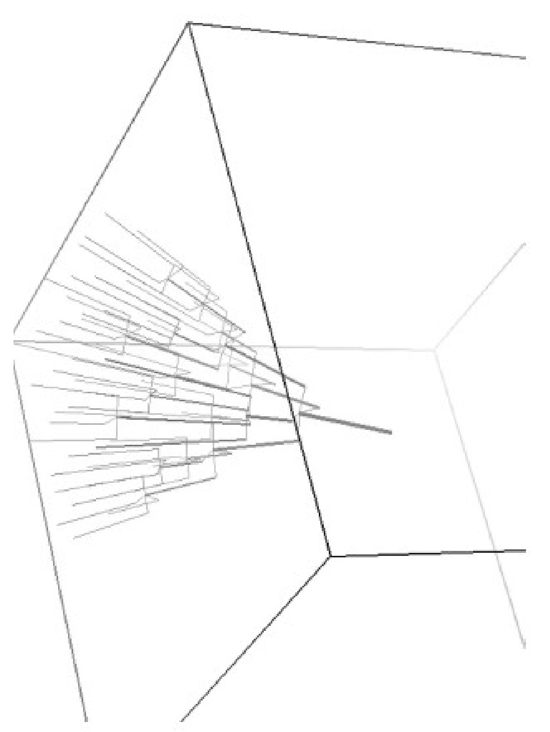

Abel & Wandelt (2002)

Numerical treatment and transport of ionizing photons

Ray Splitting

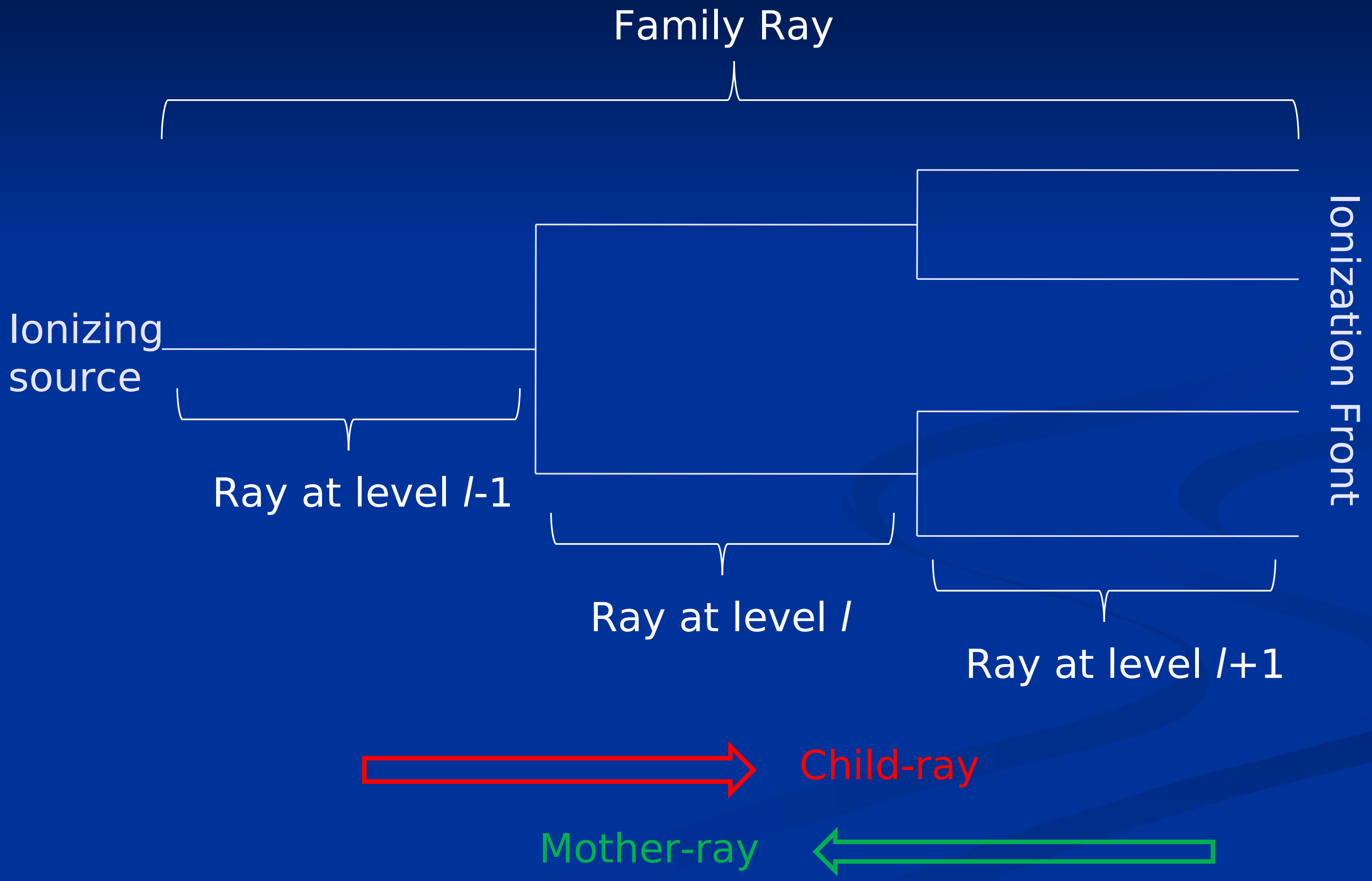

Family Ray

Ionizing source

Ray at level *l*-1

Ray at level *l*

Ray at level *l*+1

Ionization Front

Child-ray

Mother-ray

Numerical treatment and transport of ionizing photons

Ray Splitting

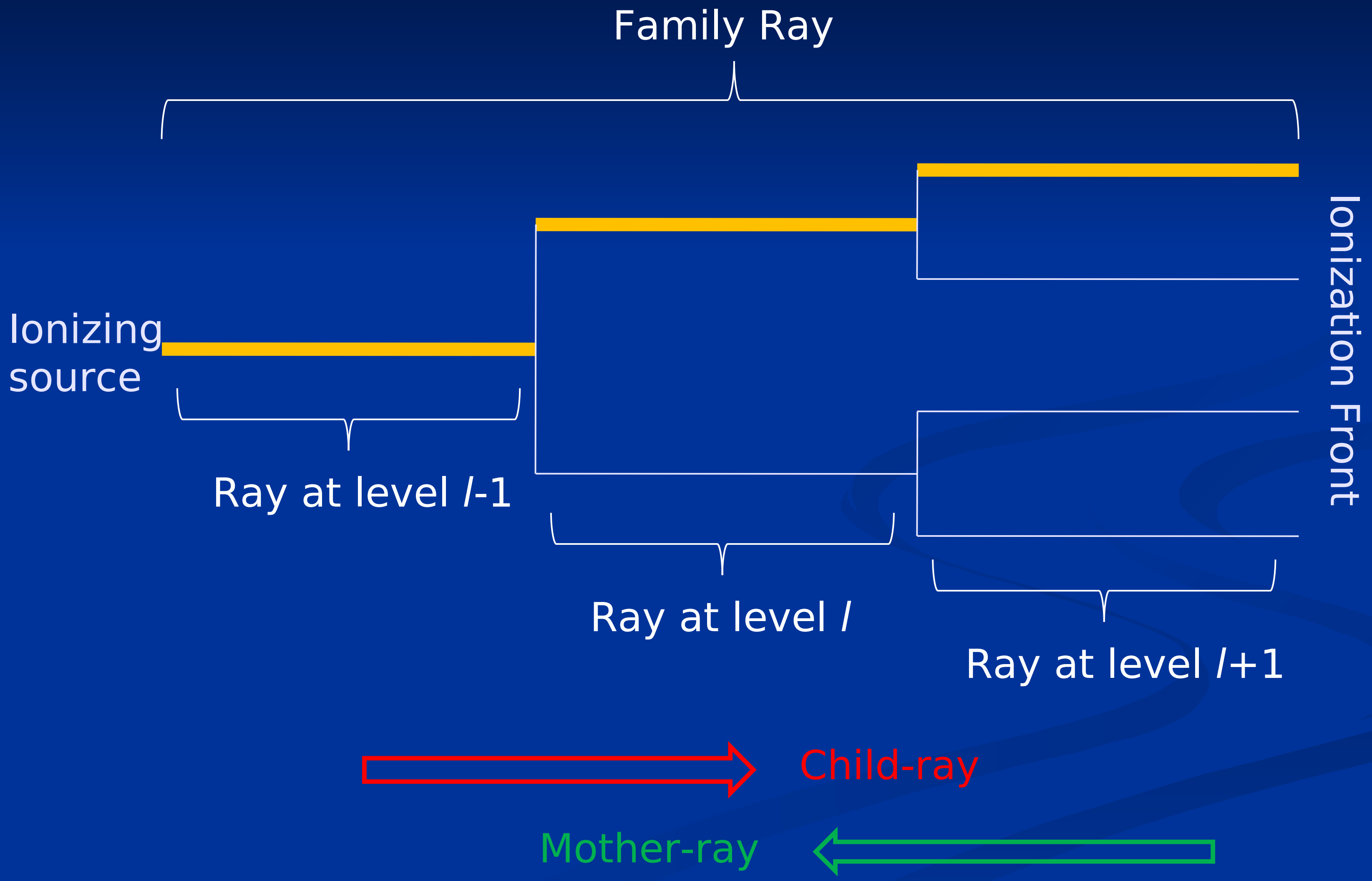

Family Ray

Ionizing source

Ray at level *l*-1

Ray at level *l*

Ray at level *l*+1

Ionization Front

Child-ray

Mother-ray

Numerical treatment and transport of ionizing photons

Ray Splitting

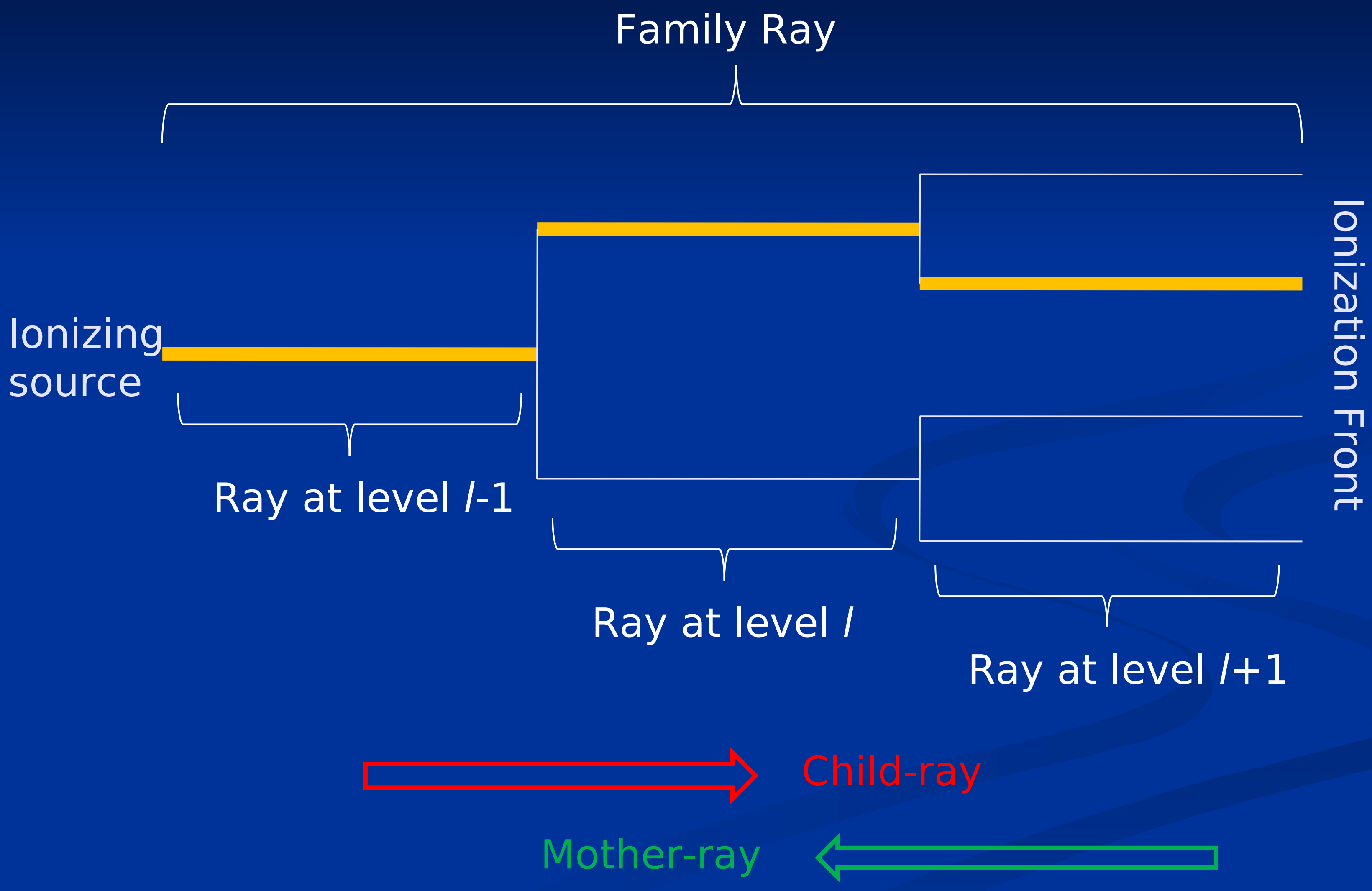
Family Ray
Ionizing source
Ionization Front
Ray at level *l*-1
Ray at level *l*
Ray at level *l*+1
Child-ray
Mother-ray

Numerical treatment and transport of ionizing photons

Ray Splitting

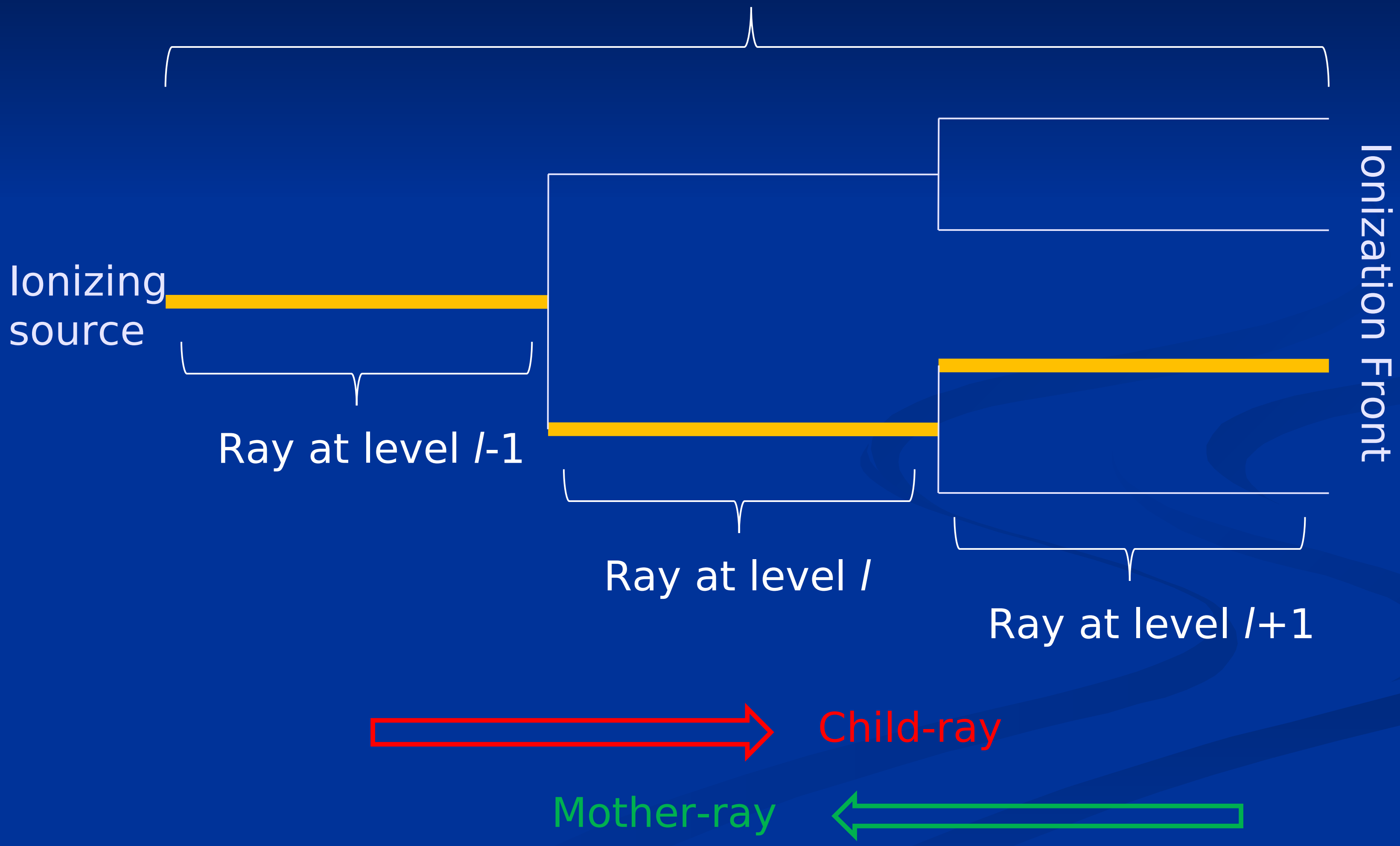

Family Ray

Ionizing source

Ray at level *l*-1

Ray at level *l*

Ray at level *l*+1

Ionization Front

Child-ray

Mother-ray

Numerical treatment and transport of ionizing photons

Ray Splitting

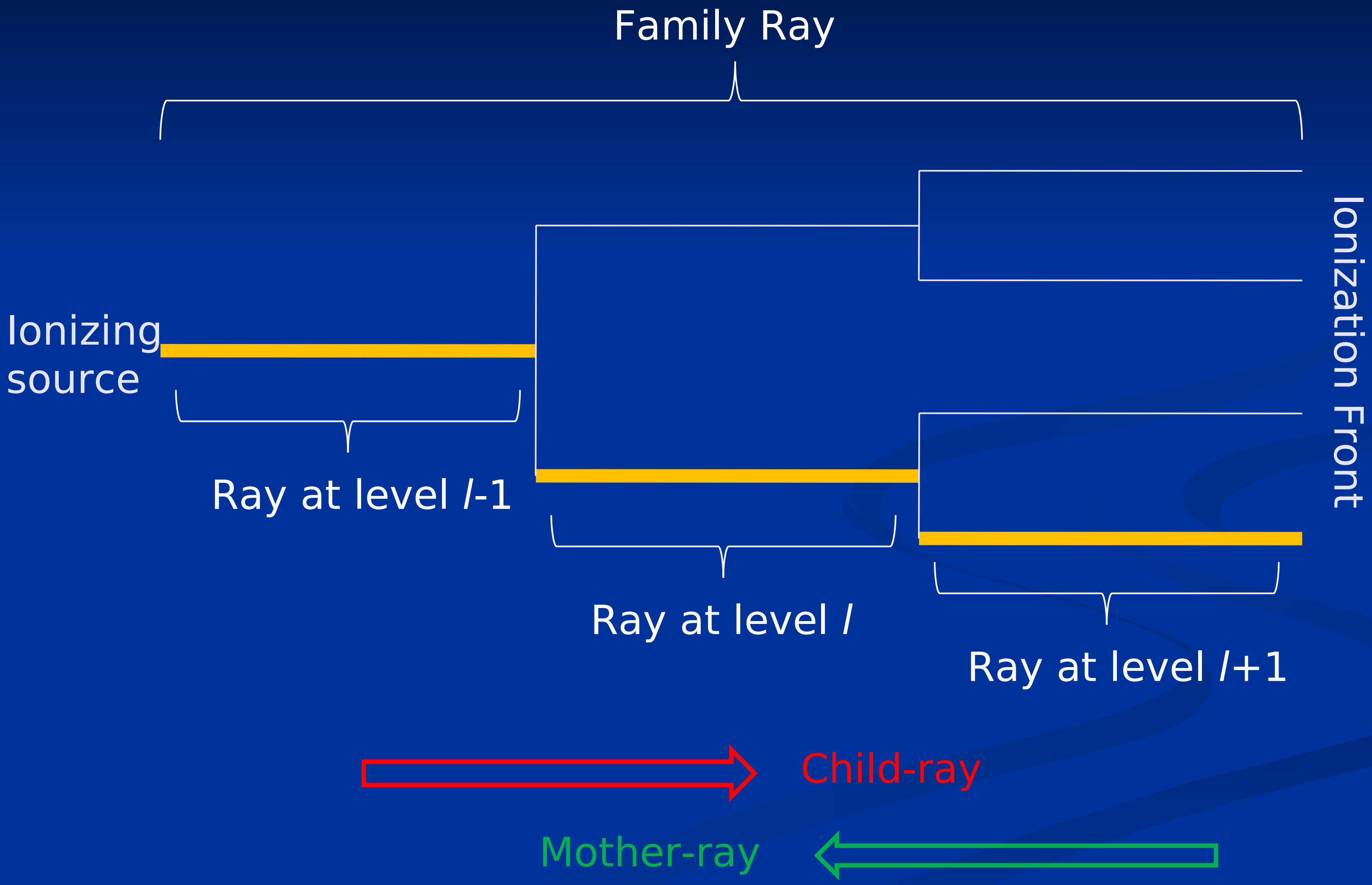

Family Ray

Ionizing source

Ionization Front

Ray at level *l*-1

Ray at level *l*

Ray at level *l*+1

Child-ray

Mother-ray

Numerical treatment and transport of ionizing photons

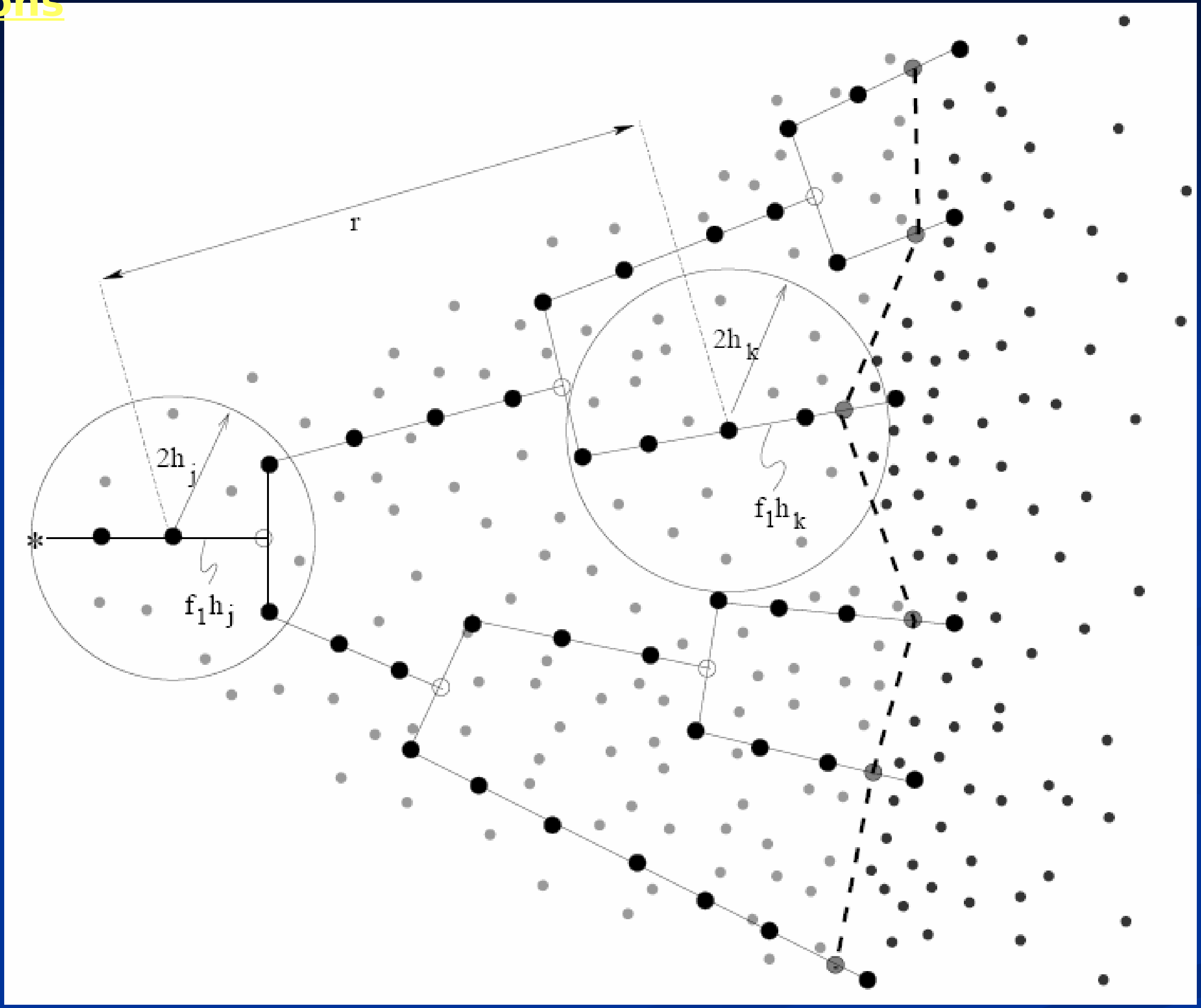
r
2h_j
f_1h_j
2h_k
f_1h_k
*

Bisbas et al. (2009)

Description of the simulations

Description of the simulations

Bonnor-Ebert sphere

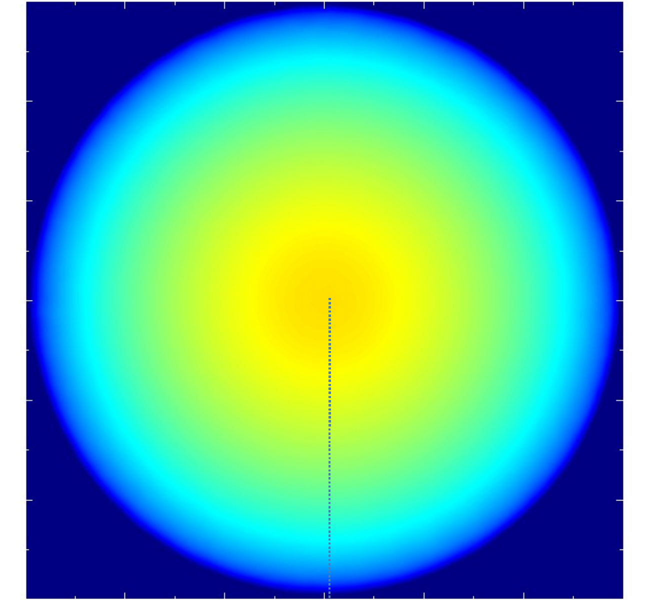

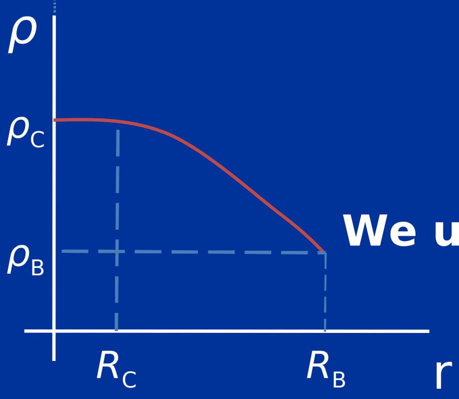

The dimensionless radius ξ_B is

$$\xi_B = \frac{R_B}{R_c}$$

where R_B is the radius of the sphere,
R_C is the radius of the core which reads

$$R_c = \frac{c_s}{\sqrt{4\pi G\rho_c}}$$

and ρ_C is the density at the centre of the sphere.

Stability analysis show that for $\xi_B < 6.451$ the sphere is stable and for $\xi_B > 6.451$ it is unstable.

We use stable Bonnor-Ebert spheres with $\xi_B = 4$

Description of the simulations

We use a barotropic equation of state of the form

$$P = c_s^2 \rho \left[1 + \left(\frac{\rho}{\rho_{\rm CRIT}} \right)^{\gamma - 1} \right]$$

where

P s the thermal pressure of the gas

ρ s the density of the gas

$\rho_{\rm CRIT}$ s the critical density

c_s s the sound speed fo $\rho \ll \rho_{\rm CRIT}$

γ s the ratio of specific heats

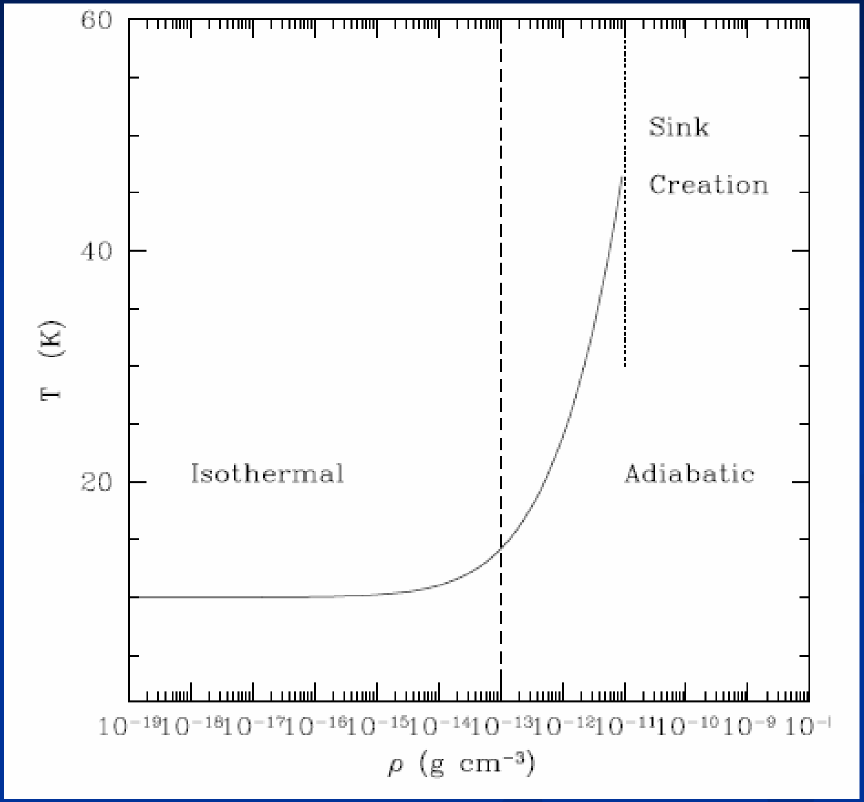

The temperature of the gas is

$$T = T_{\rm iso} \left[1 + \left(\frac{\rho}{\rho_{\rm CRIT}} \right)^{\gamma - 1} \right]$$

where

$T_{\rm iso}$ the temperature of the gas at low densities

Description of the simulations

We introduce the dimensionless param $\lambda \equiv \frac{D}{R}$ and we run simulations for λ = 2, 5, 10.

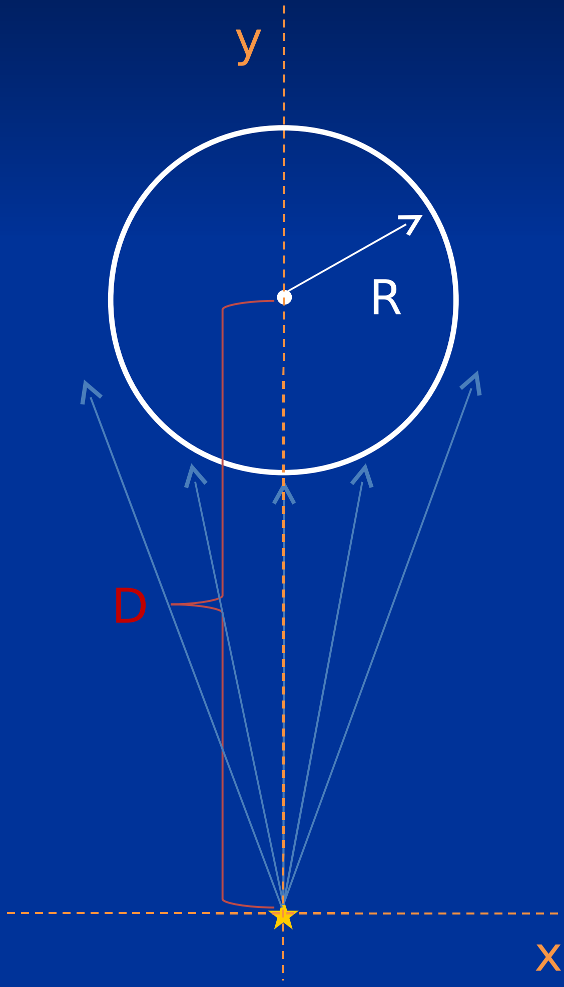

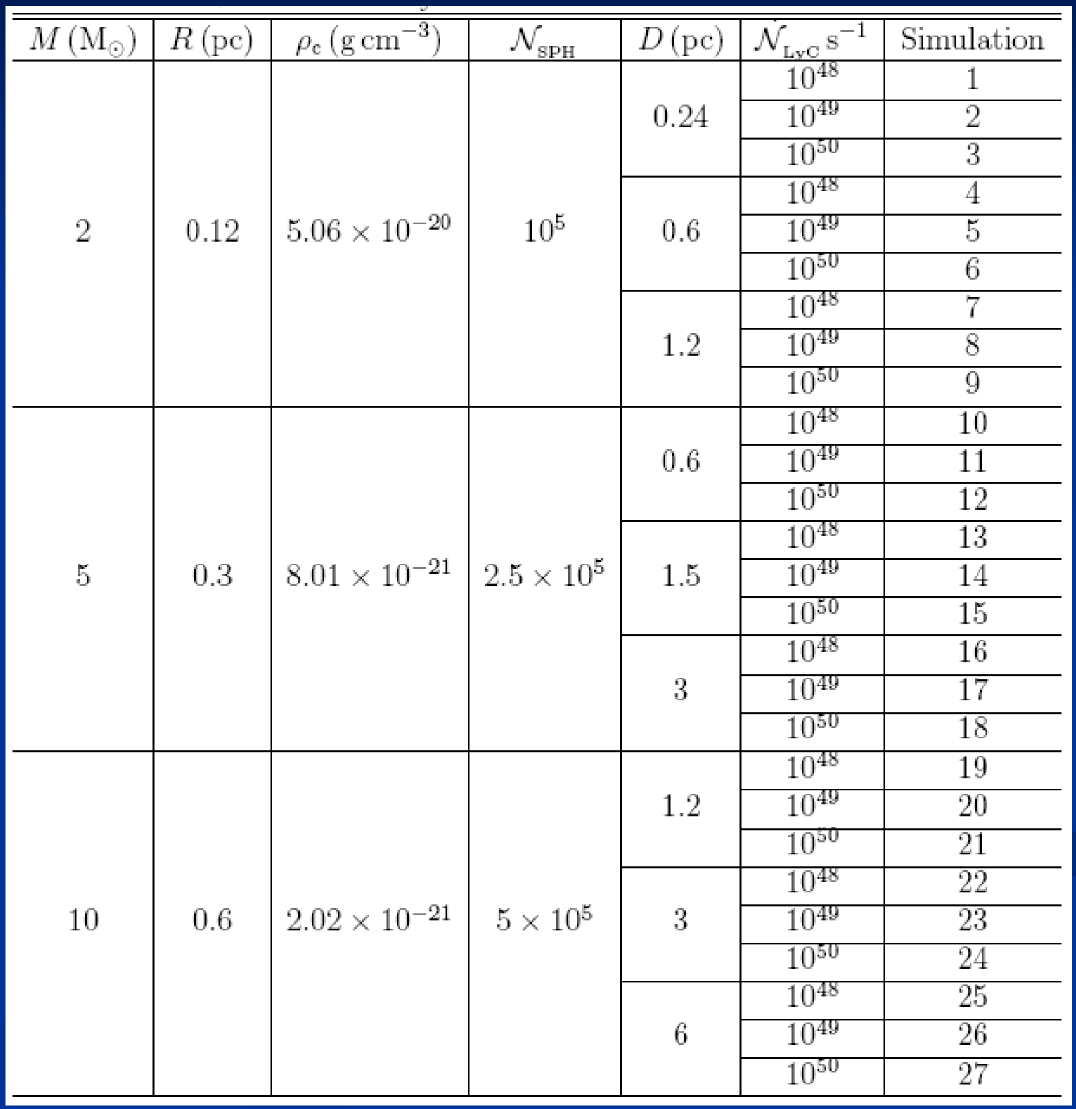

$M\,(\mathrm{M}_\odot)$	$R\,(\mathrm{pc})$	$\rho_c\,(\mathrm{g\,cm^{-3}})$	$\mathcal{N}_{\mathrm{SPH}}$	$D\,(\mathrm{pc})$	$\dot{\mathcal{N}}_{\mathrm{LyC}}\,\mathrm{s^{-1}}$	Simulation
2	0.12	5.06×10^{-20}	10^5	0.24	10^{48}	1
					10^{49}	2
					10^{50}	3
				0.6	10^{48}	4
					10^{49}	5
					10^{50}	6
				1.2	10^{48}	7
					10^{49}	8
					10^{50}	9
5	0.3	8.01×10^{-21}	2.5×10^5	0.6	10^{48}	10
					10^{49}	11
					10^{50}	12
				1.5	10^{48}	13
					10^{49}	14
					10^{50}	15
				3	10^{48}	16
					10^{49}	17
					10^{50}	18
10	0.6	2.02×10^{-21}	5×10^5	1.2	10^{48}	19
					10^{49}	20
					10^{50}	21
				3	10^{48}	22
					10^{49}	23
					10^{50}	24
				6	10^{48}	25
					10^{49}	26
					10^{50}	27

Description of the simulations

We define here the terminology that we will use in our discussion. We call:

Star Formation (SF): when the clump during the compression becomes gravitationally unstable and forms stars

Acceleration (A): when the clump does not become gravitationally unstable during the compression and it simply re-expands and evaporates

Evaporation (E): when the incident flux is so strong that it fully evaporates it instantly

Description of the simulations

Technical tests

We perform technical tests in order to explore the capabilities of our code in modeling star formation in clumps ionized by an external source.

In particular, we examine how the physical quantities of Bonnor-Ebert spheres, such as their morphological evolution and their star formation efficiency, are affected by the numerical noise of the calculations.

To do this, we consider the $2M_o$ Bonnor-Ebert sphere with $\lambda=2$ ($R=0.12$, $D=0.24$pc). We run 4 simulations were we perturb very little the initial positions of this sphere.

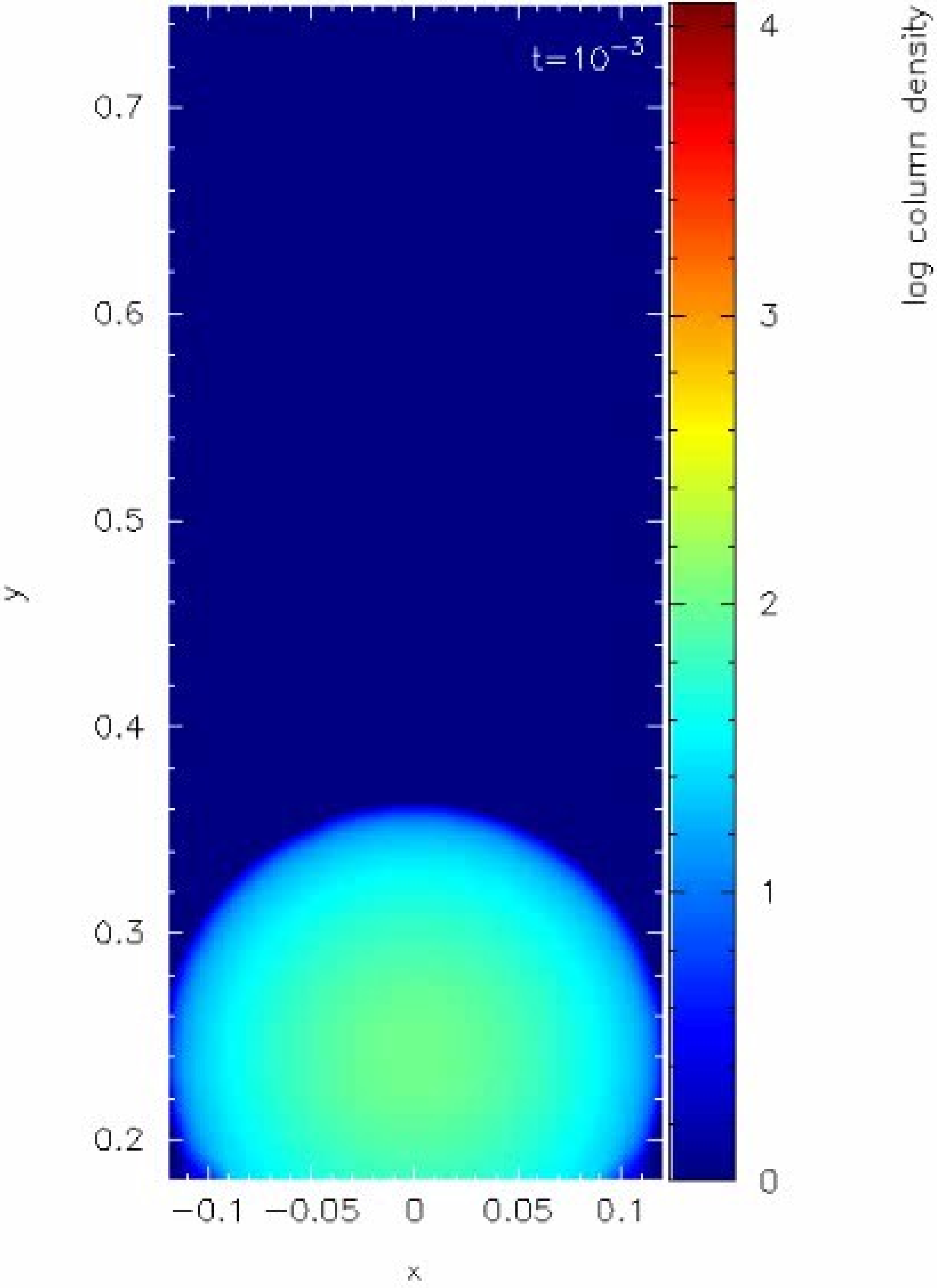
t=10^{-3}
0.7
0.6
0.5
0.4
0.3
0.2
y
−0.1
−0.05
0
0.05
0.1
x
4
3
2
1
0
log column density

Description of the simulations

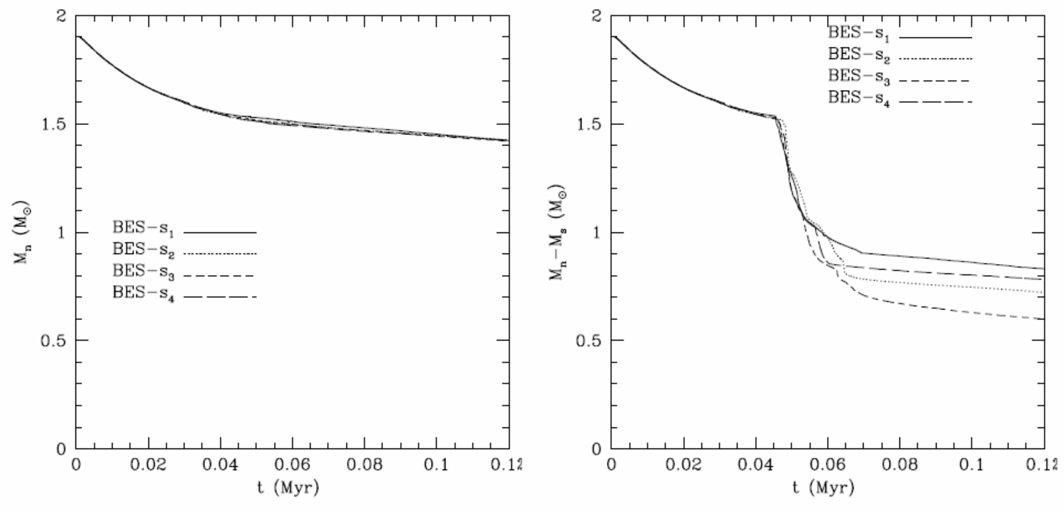

Simulation	$t_{\rm sink}$ (Myr)	$M_{\rm n,s}$ ($M_\odot$)	$N_{\rm s,tot}$	$M_{\rm s,tot}$ ($M_\odot$)
BES-s$_1$	0.0455	1.54	3	0.59
BES-s$_2$	0.0475	1.52	5	0.7
BES-s$_3$	0.0461	1.53	3	0.82
BES-s$_4$	0.0462	1.52	9	0.64

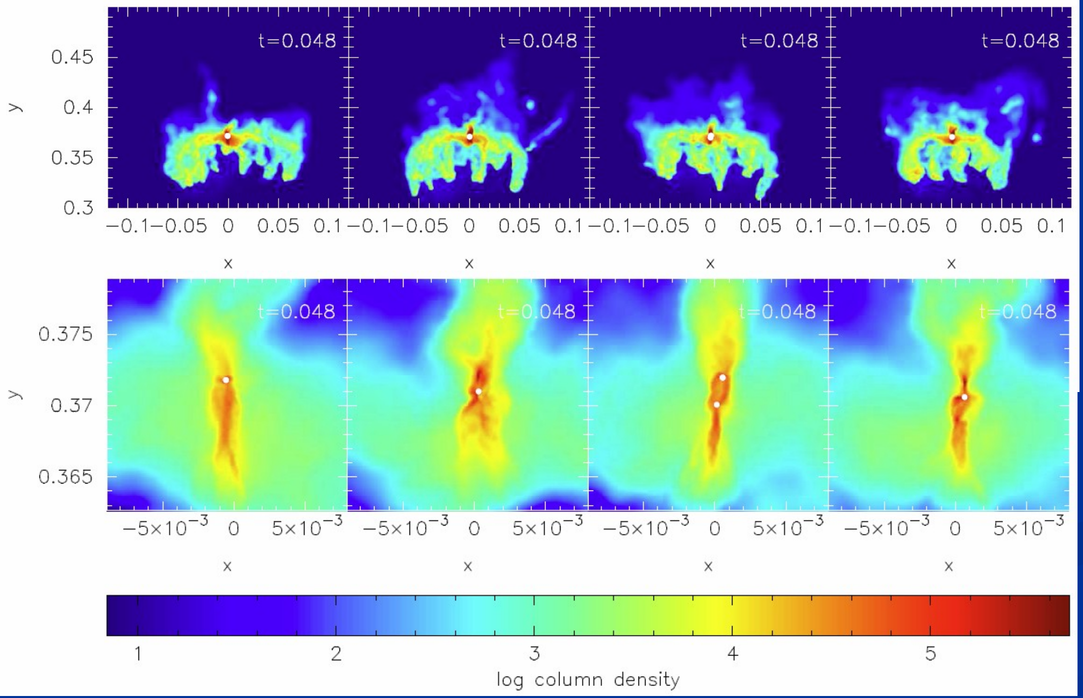

Results of technical tests

1. The sink creation time, $t_{\rm SINK}$, remains unchanged.
2. The neutral remaining mass, $M_{\rm n,s}$, $t_{\rm SINK}$ remains unchanged.
3. The total number of sink particles formed, $N_{\rm s,tot}$, strongly depends on the numerical noise.
4. The total mass of sink particles formed, $M_{\rm s,tot}$, is quite similar in all four simulations.

Results

Results

The curvature of the incident flux delays fragmentation

Since we place the Bonnor-Ebert spheres at various distances from the source, it is interesting to see how the curvature of the incident flux affects their evolution.

To do this we perform a set of three simulations where we place the $2M_o$ at various distances *D* in order to have λ = 2, 5, 10, and we keep constant the incident flux $\Phi_D = 1.45 \times 10^{11}\ \mathrm{cm}^{-2}\mathrm{s}^{-1}$.

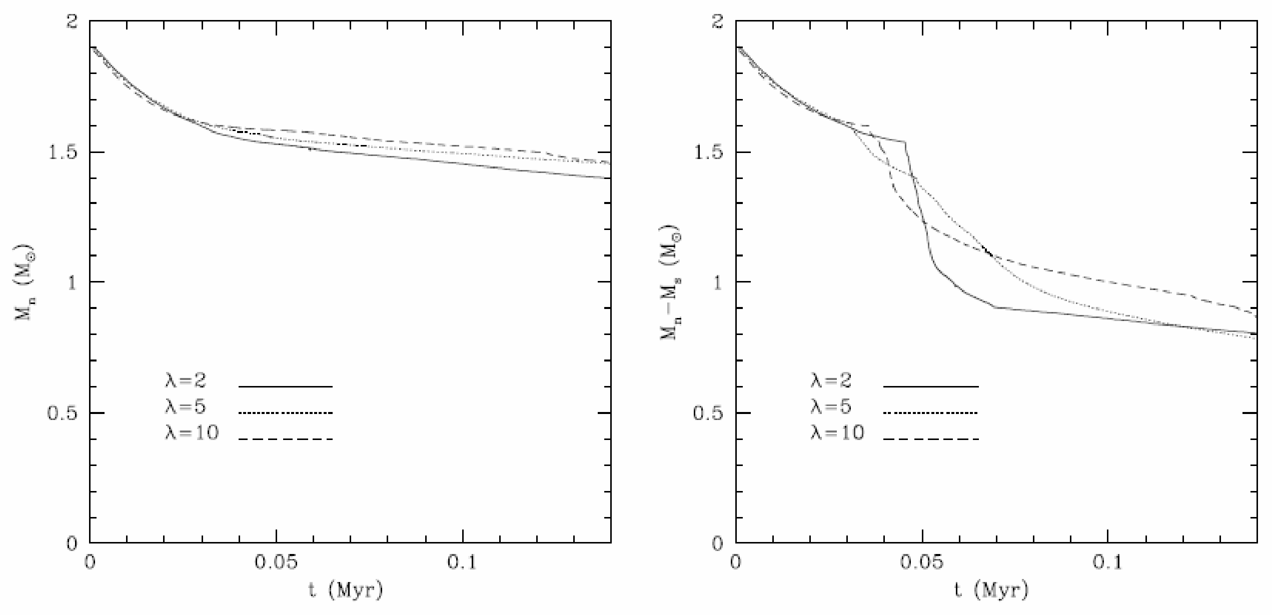

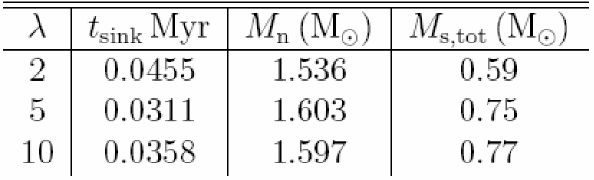

λ	$t_{\rm sink}$ Myr	$M_{\rm n}$ ($M_\odot$)	$M_{\rm s,tot}$ ($M_\odot$)
2	0.0455	1.536	0.59
5	0.0311	1.603	0.75
10	0.0358	1.597	0.77

Results

The curvature of the incident flux delays fragmentation

λ=10

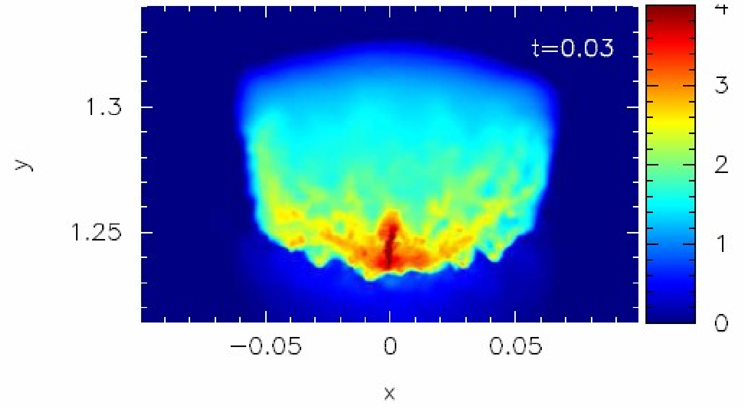

λ=5

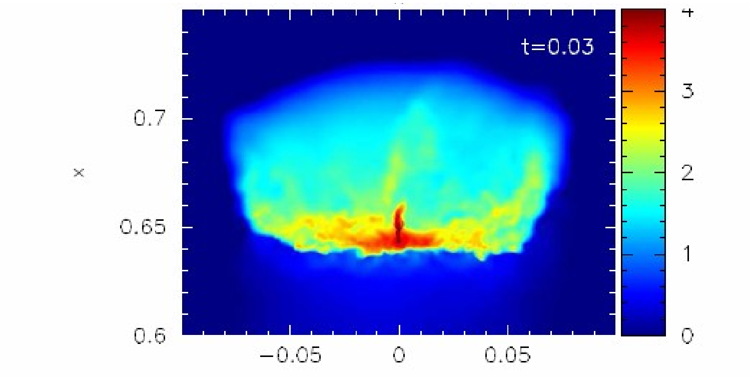

λ=2

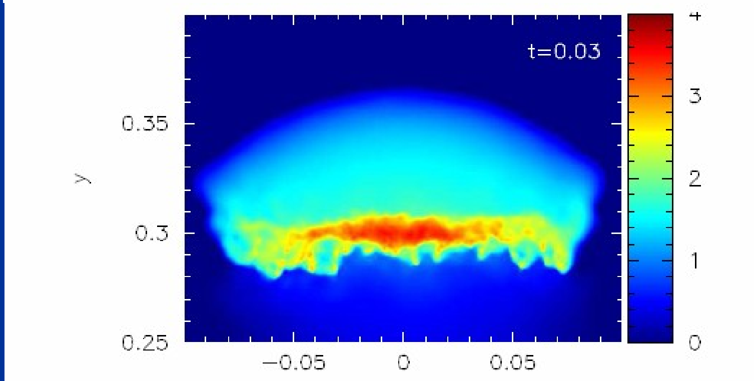

λ=2 λ=10

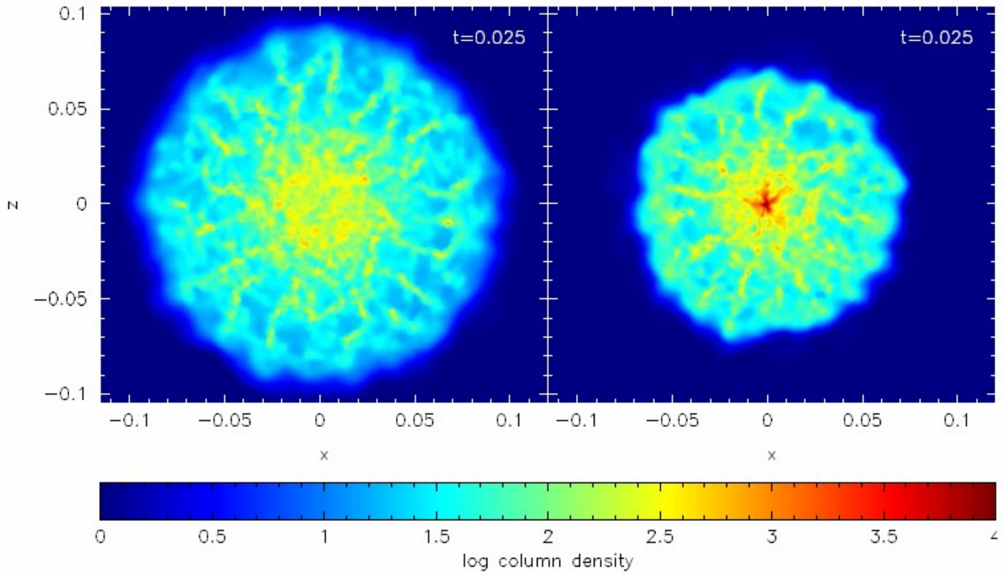

Observe that the surface density of the shocked core is lower for lower λ, and therefore the gravitational forces in the layer are weaker.

In addition, the shocked material has a greater tangential divergence for lower λ.

Both these factors act to delay fragmentation, and hence also sink creation, when is small

Results

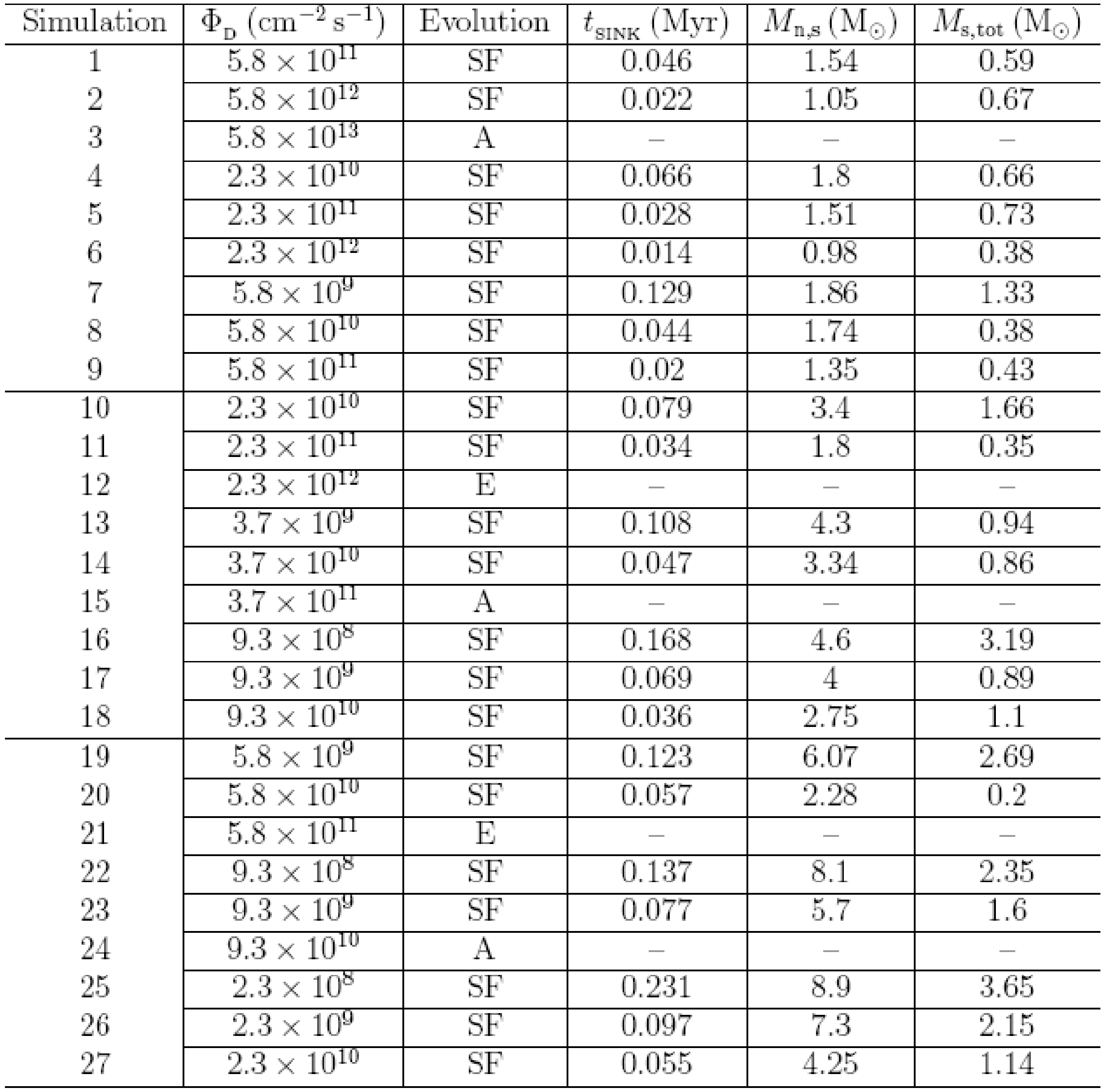

Simulation	$\Phi_{\rm D}$ (cm^{-2} s^{-1})	Evolution	$t_{\rm SINK}$ (Myr)	$M_{\rm n,s}$ (M$_\odot$)	$M_{\rm s,tot}$ (M$_\odot$)
1	5.8×10^{11}	SF	0.046	1.54	0.59
2	5.8×10^{12}	SF	0.022	1.05	0.67
3	5.8×10^{13}	A	–	–	–
4	2.3×10^{10}	SF	0.066	1.8	0.66
5	2.3×10^{11}	SF	0.028	1.51	0.73
6	2.3×10^{12}	SF	0.014	0.98	0.38
7	5.8×10^{9}	SF	0.129	1.86	1.33
8	5.8×10^{10}	SF	0.044	1.74	0.38
9	5.8×10^{11}	SF	0.02	1.35	0.43
10	2.3×10^{10}	SF	0.079	3.4	1.66
11	2.3×10^{11}	SF	0.034	1.8	0.35
12	2.3×10^{12}	E	–	–	–
13	3.7×10^{9}	SF	0.108	4.3	0.94
14	3.7×10^{10}	SF	0.047	3.34	0.86
15	3.7×10^{11}	A	–	–	–
16	9.3×10^{8}	SF	0.168	4.6	3.19
17	9.3×10^{9}	SF	0.069	4	0.89
18	9.3×10^{10}	SF	0.036	2.75	1.1
19	5.8×10^{9}	SF	0.123	6.07	2.69
20	5.8×10^{10}	SF	0.057	2.28	0.2
21	5.8×10^{11}	E	–	–	–
22	9.3×10^{8}	SF	0.137	8.1	2.35
23	9.3×10^{9}	SF	0.077	5.7	1.6
24	9.3×10^{10}	A	–	–	–
25	2.3×10^{8}	SF	0.231	8.9	3.65
26	2.3×10^{9}	SF	0.097	7.3	2.15
27	2.3×10^{10}	SF	0.055	4.25	1.14

Results

Snapshots were taken at sink creation tt_{SINK}

$M = 2\ \mathrm{M_o}$

↓

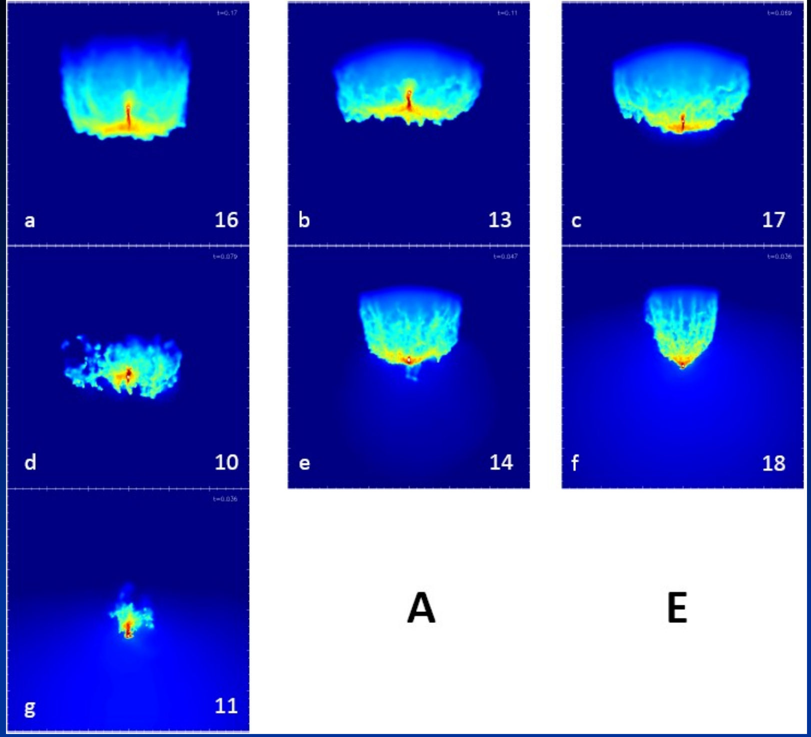

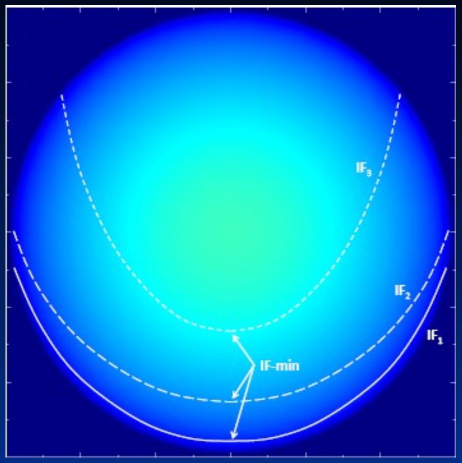
IF$_3$
IF$_2$
IF$_1$
IF-min

$M = 10\ \mathrm{M_o}$

↓

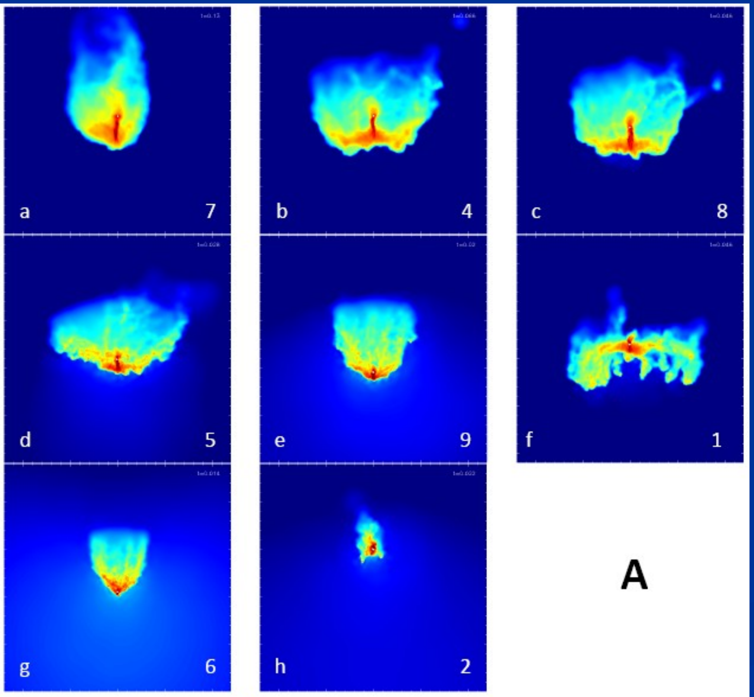

↑

$M = 5\ \mathrm{M_o}$

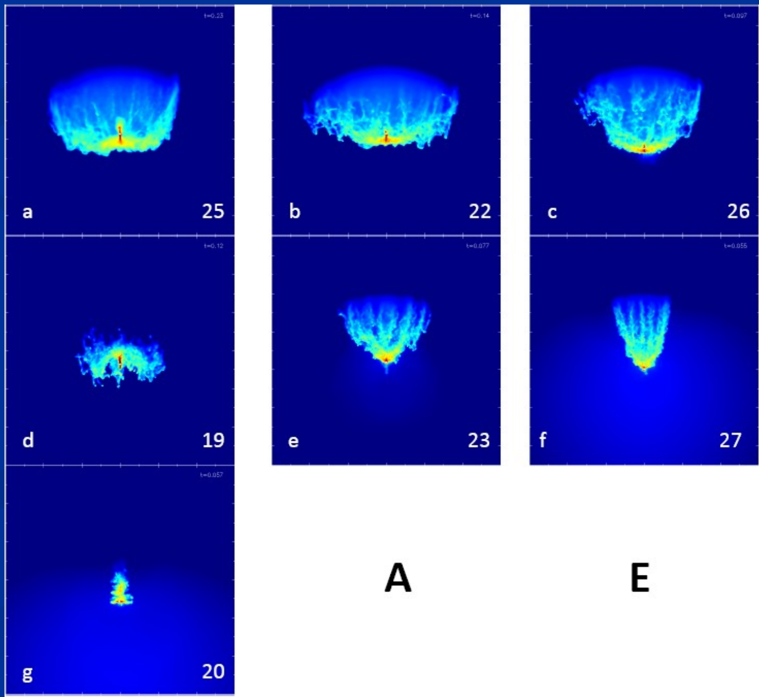

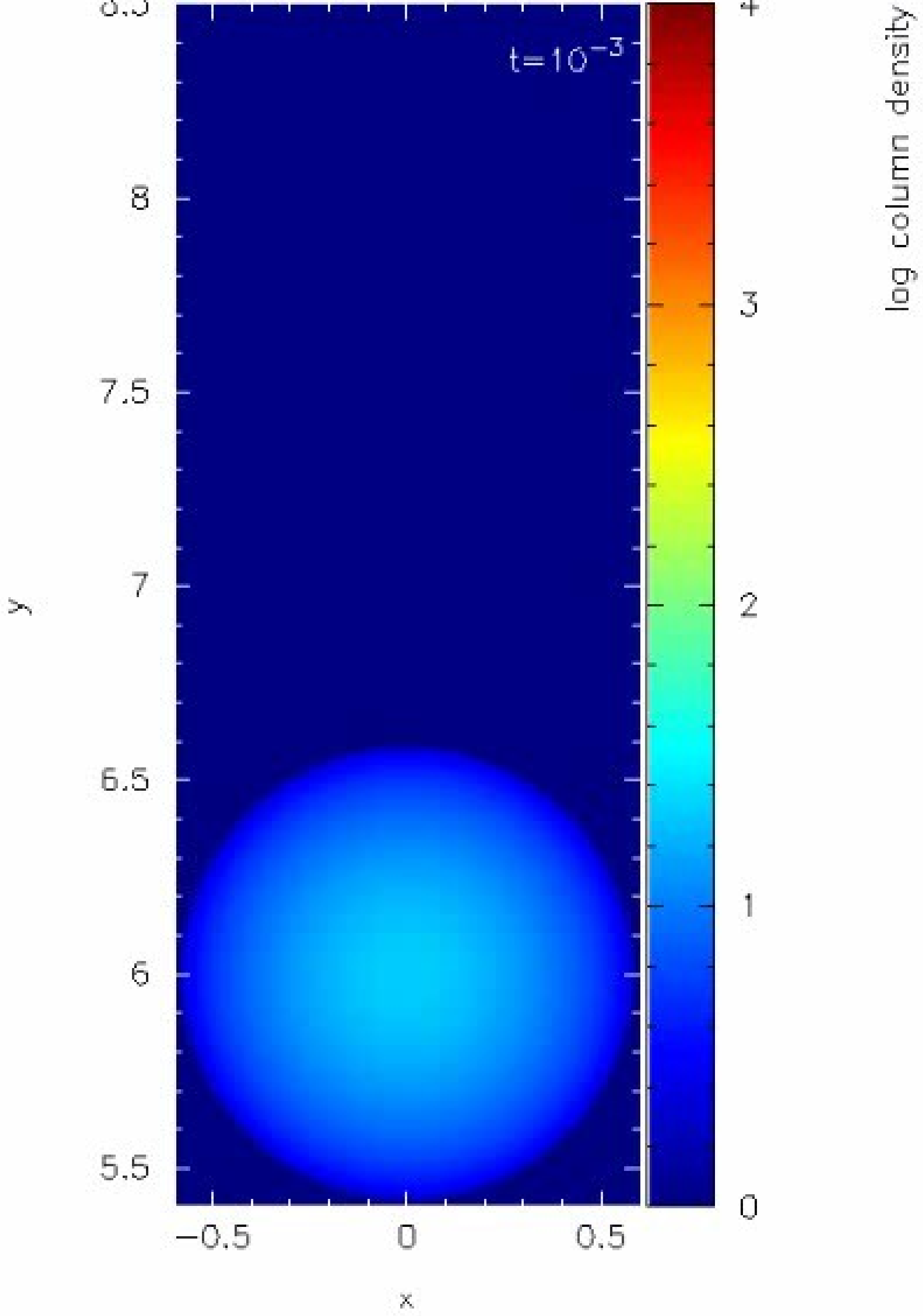
t=10^{-3}
8.5
8
7.5
7
6.5
6
5.5
y
−0.5
0
0.5
x
4
3
2
1
0
log column density

Results

The flux-mass diagram

Semi-logarithmic diagram where we define the zones `Star Formation', `Acceleration', and `Evaporation’.

The logarithmic *x*-axis of this diagram is the incident flux (log Φ) and the *y*-axis is the initial mass *M* of the clump.

From these simulations it is not possible to define the exact location for the transition of one zone to another.

However, it is clear that as the mass *M* of these Bonnor-Ebert spheres decreases, they appear to survive more in higher fluxes.

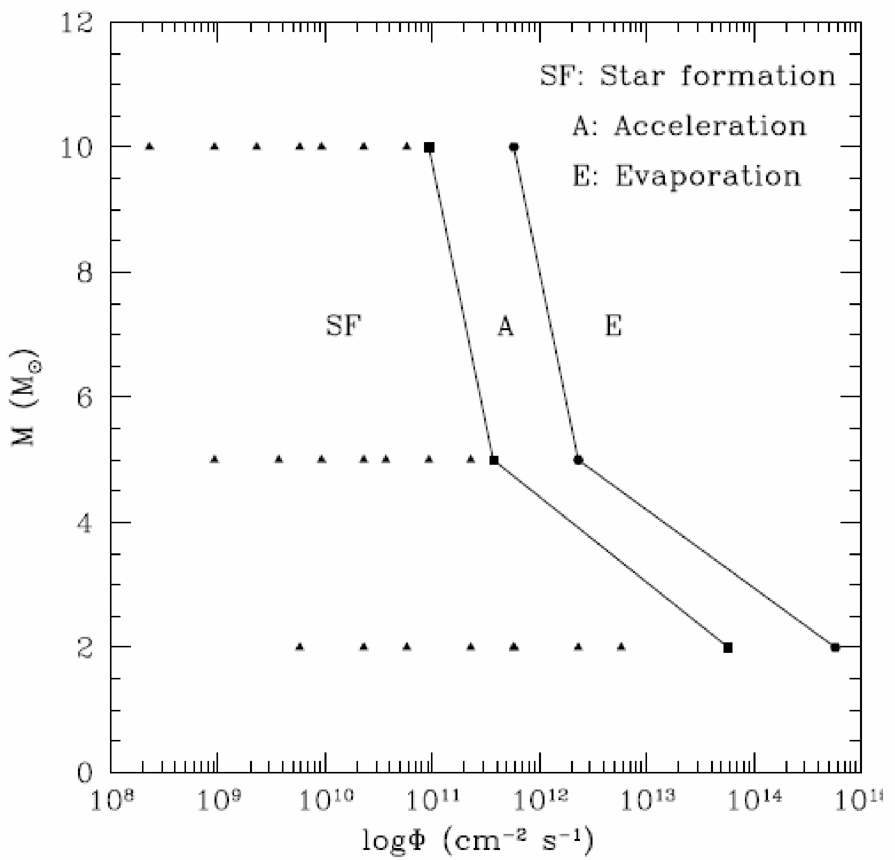

Results

Stars form close to the periphery with increasing the flux

A common feature amongst the morphological structures at sink creation time, is that stars form along the line of sight towards the exciting star (agreement with *Sugitani et al. 1999*)

We define d_t as the distance of the first sink particle formed from the ionization front. We plot d_t/R versus *Φ.*

We omit the simulations with the irregular jelly-fish structu-re.

$M = 2$ M$_o$

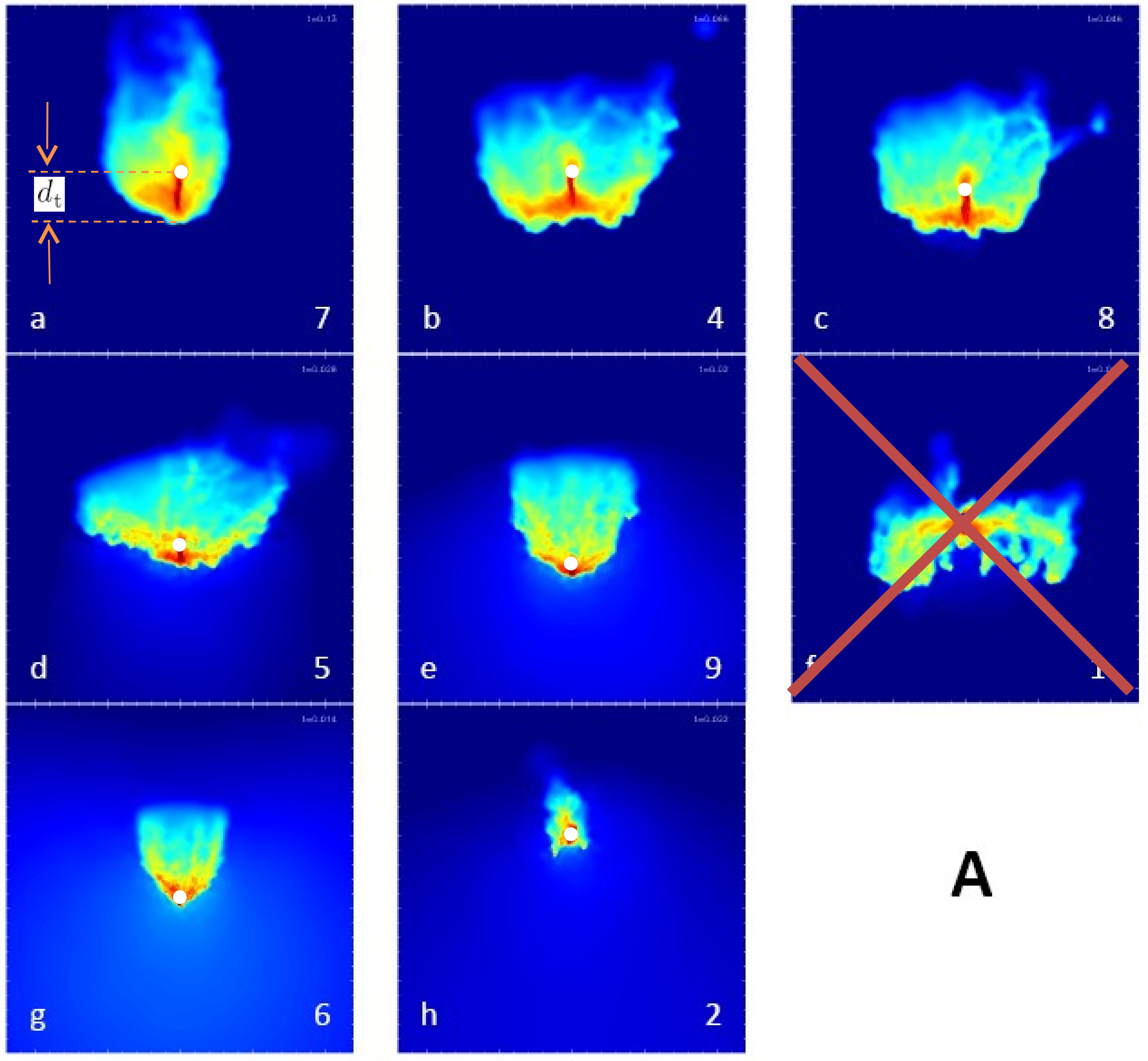

Results

Stars form close to the periphery with increasing the flux

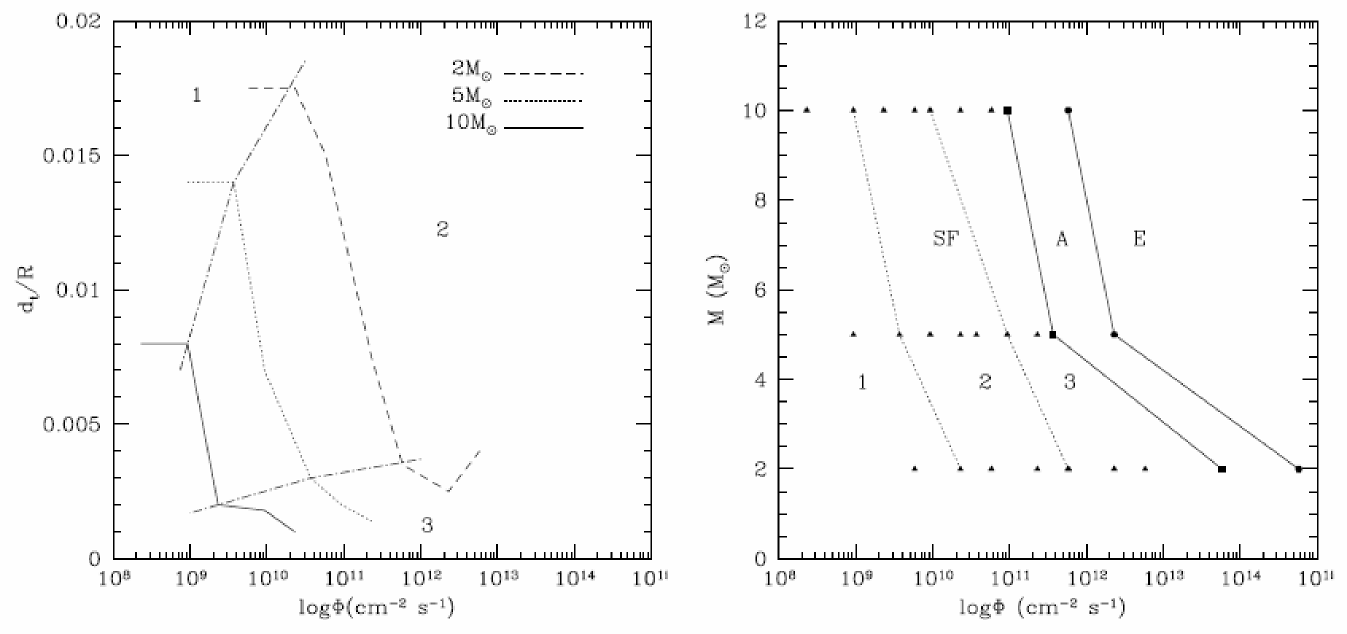

The first zone (1) corresponds to low fluxes. Here, stars tend to form along the filamentary structure and particularly at its innermost part.

The second zone (2) corresponds to intermediate fluxes. Here, the filament becomes smaller and therefore stars tend to form closer to the periphery.

Finally, the third zone (3) corresponds to high fluxes. The filamentary structure here cannot be developed and therefore stars are formed *at* the periphery.

Results

Stars form during maximum compression with increasing the flux

We define w_d as the width of the two sides of each clump and we normalize it with the initial radius of each Bonnorw_d/Rrt sphere, . This value represents the measure of compression.

We plot w_d/R versus the incident flux Φ.

We omit the simulations with the irregular jelly-fish structu-re.

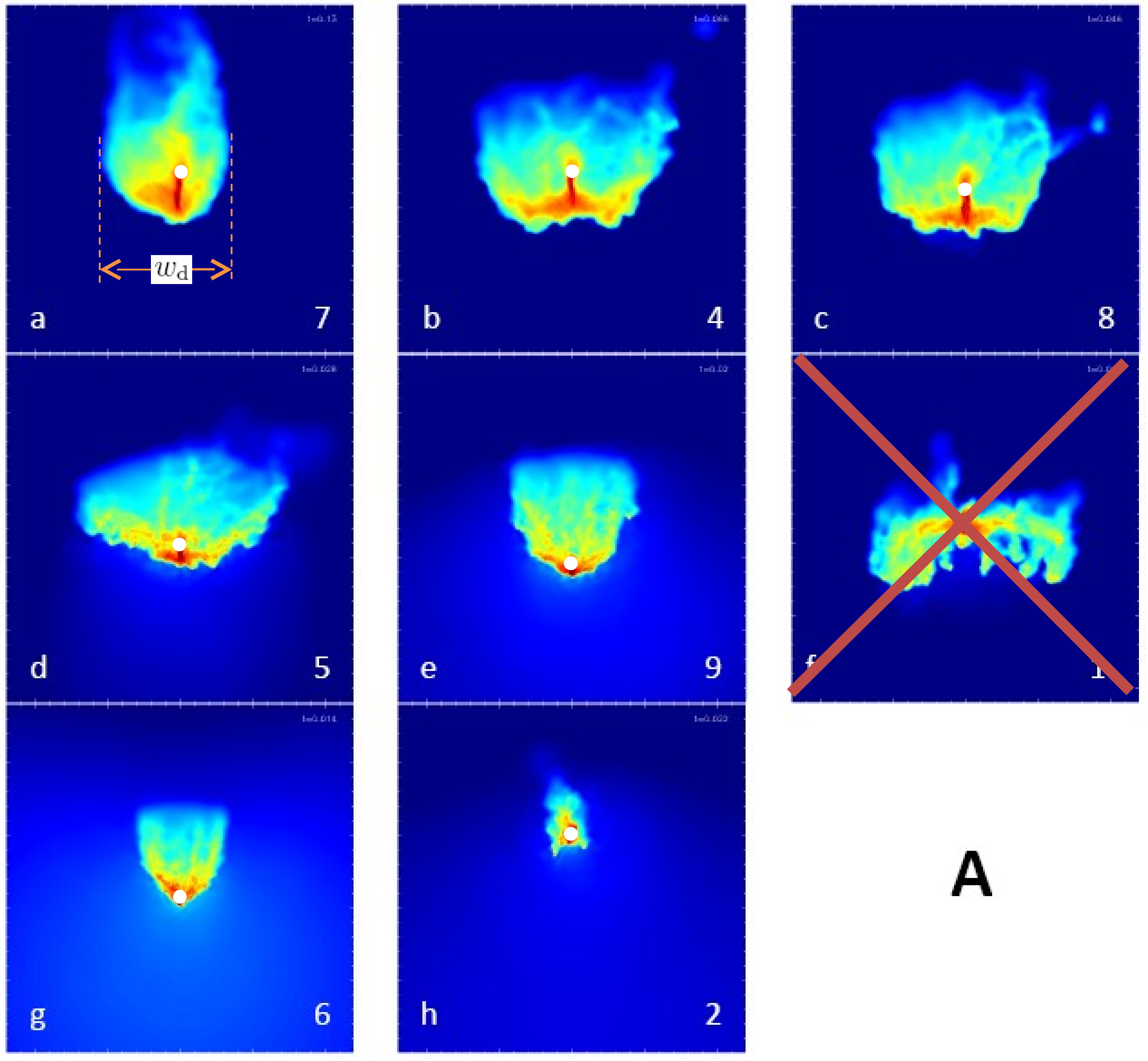

$M = 2\ \mathrm{M}_\mathrm{o}$

Results

Stars form during maximum compression with increasing the flux

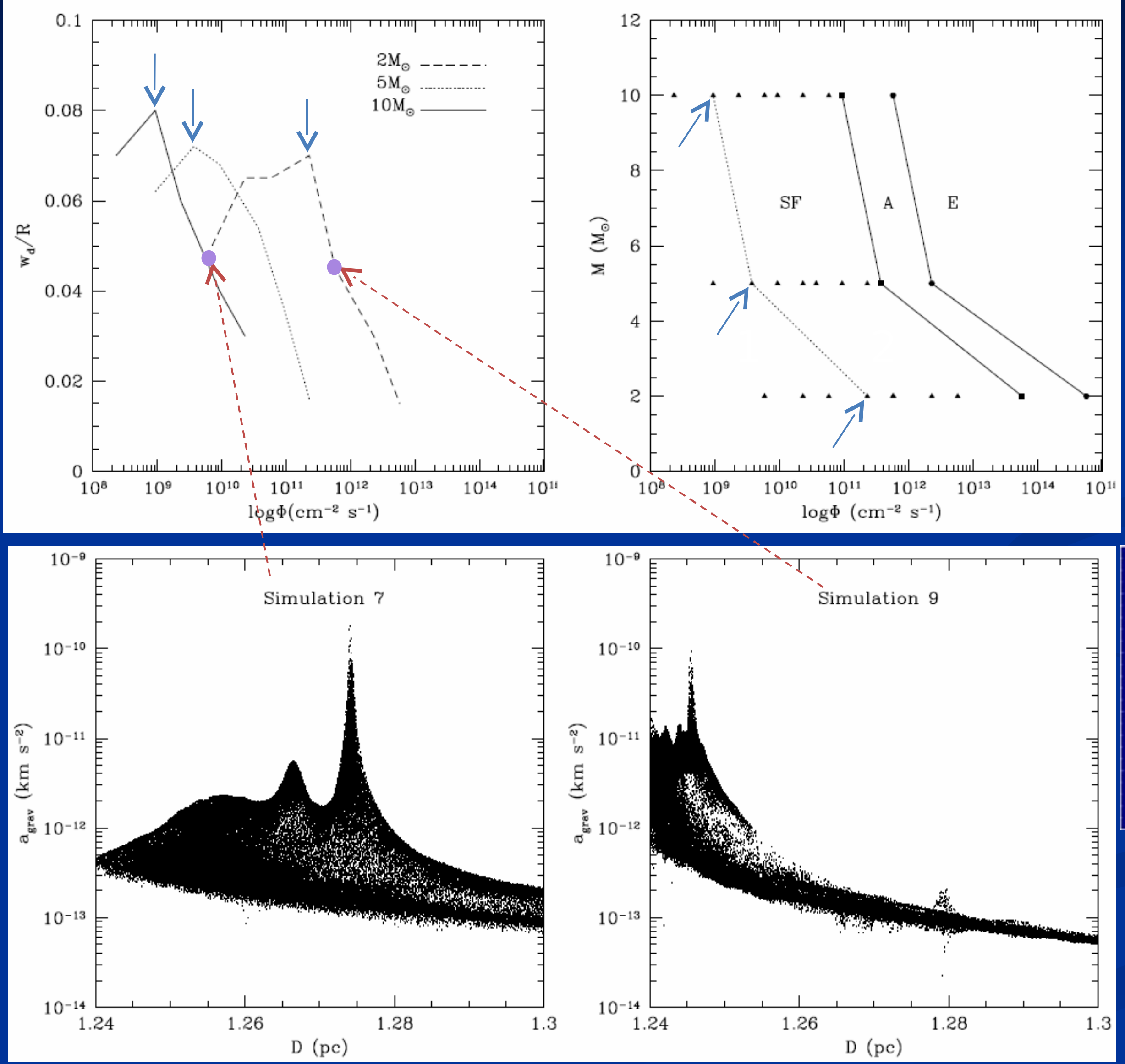

Compression is a result of:

Zone 1: Ionization + Gravity

Zone 2: Ionization only

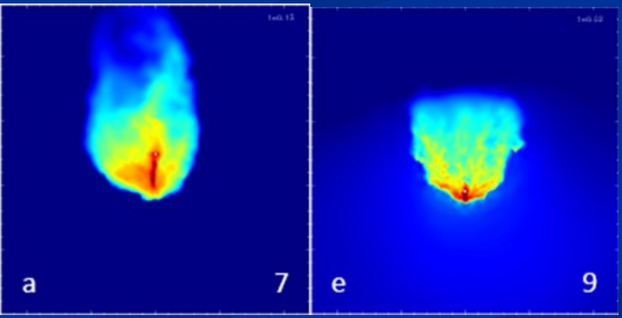

$$a_{\text{grav}} = \sqrt{a_x^2 + a_y^2 + a_z^2}$$

Results

Low fluxes increase the total mass of stars

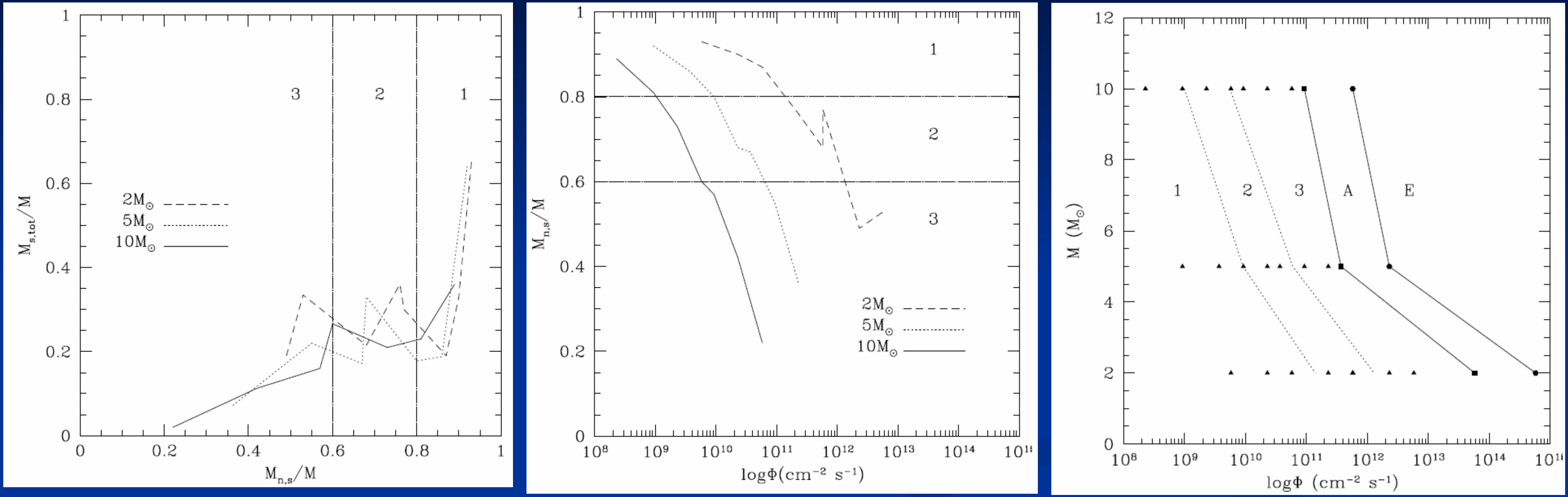

Zone 1: Stars formed at the innermost regions. Compression is supported by ionization and mutual gravity. Low fluxes favour the total final mass of the sink particles.

Zone 2: Stars tend to form closer to the periphery. Compression is supported by ionization only. Intermediate fluxes form stars with total mass about 30% of the initial mass of the clumps.

Zone 3: Stars formed at the periphery. Compression is supported by ionization only. High fluxes act to form stars with low total mass.

Conclusions

Conclusions

We examined clumps of various masses and fluxes of various intensities. In general we find a connection between the incident flux and the corresponding star formation efficiency. We propose a *flux-mass diagram* to map the resultant production of each simulation. Our results can be summarized as follows:

Low fluxes: An extended filamentary structure develops. Stars tend to form at its innermost part. The filament increases the mutual gravitational forces of the initial clump which increase its compression. The total final mass of stars is high comparing with the initial mass of the clump.

Intermediate fluxes: The filamentary structure is small. Morphology is close to **U**-shape. Stars tend to form closer to the periphery. Ionization starts to be the dominant factor of compressing the initial clump. The total final mass of stars is about 30% of the initial mass of the clump.

High fluxes: No filamentary structure. Morphology is close to **V**-shape. Stars form at the periphery. Ionization is the dominant factor of compression. The total final mass of stars is very low.

Very high fluxes: No star formation. The clumps are being accelerated and evaporated.

References

Abel, T., & Wandelt, B.D. 2002, MNRAS, 330, L53
Bertoldi, F. 1989, ApJ, 346, 735
Bisbas, T. G., Wunsch, R., Whitworth, A. P., & Hubber, D. A., 2009, A&A, 497, 649
Dale, J.E., Bonnell, I. A., Clarke, C. J., & Bate, M. R. 2005, MNRAS, 358, 291
Deharveng, L., Zavagno, A., & Caplan, J. 2005, A&A, 433, 565
Gorski, K. M., Hivon, E., Banday, A. J., Wandelt, B. D., Hansen, F. K., *et al*. 2005, ApJ, 622, 759
Gritschneder, M., Naab, T., Burkert, A., Walch, S., Heitsch, F., & Wertzstein, M. 2009, MNRAS, 339, 21
Henney, W. J., Arthur, S. J., De Colle, F., & Mellema, G. 2009, MNRAS, 398, 157
Hubber et al. 2009, *in preparation*
Kessel-Deynet, O., & Burkert, A. 2003, MNRAS, 338, 545
Lefloch, B., & Lazareff, B. 1994, A&A, 289, 559
Lefloch, B., & Lazareff, B. 1995, A&A, 301, 522
Lefloch, B., Lazareff, B., & Castets, A. 1997, A&A, 324, 249
Miao, J., White, G. J., Nelson, R., Thompson, M., & Morgan, L. 2006, MNRAS, 369, 143
Miao, J., White, G. J., Thompson, M. A., & Nelson, R. P. 2009, ApJ, 692, 382
Morgan, L. K., Thompson, M. A., Urquhart, J. S., & White, G. J. 2008, A&A, 477, 577
Price, D. J. 2007, Publications of the Astronomical Society of Australia, 24, 159
Sandford, M. T., II, Whitaker, R. W., & Klein, R. I. 1982, ApJ, 260, 183
Sugitani, K., Tamura, M., & Ohura, K. 1999, Star Formation 1999, Proceedings of Star Formation 1999, held in Nagoya, Japan, June 21-25, 1999, Editor: T. Nakamoto, Nobeyama Radio Observatory, p. 358-364, 358.

EXTRA SLIDES BEYOND THIS POINT

Profile of the simulations

Uniform density

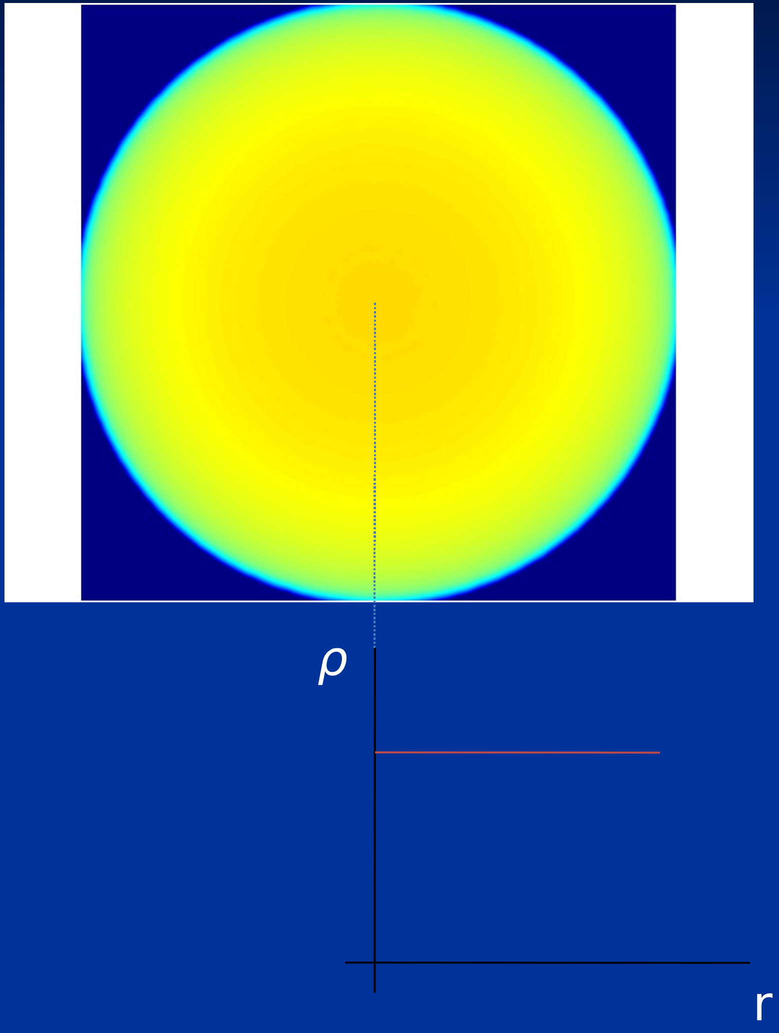

Bonnor-Ebert sphere

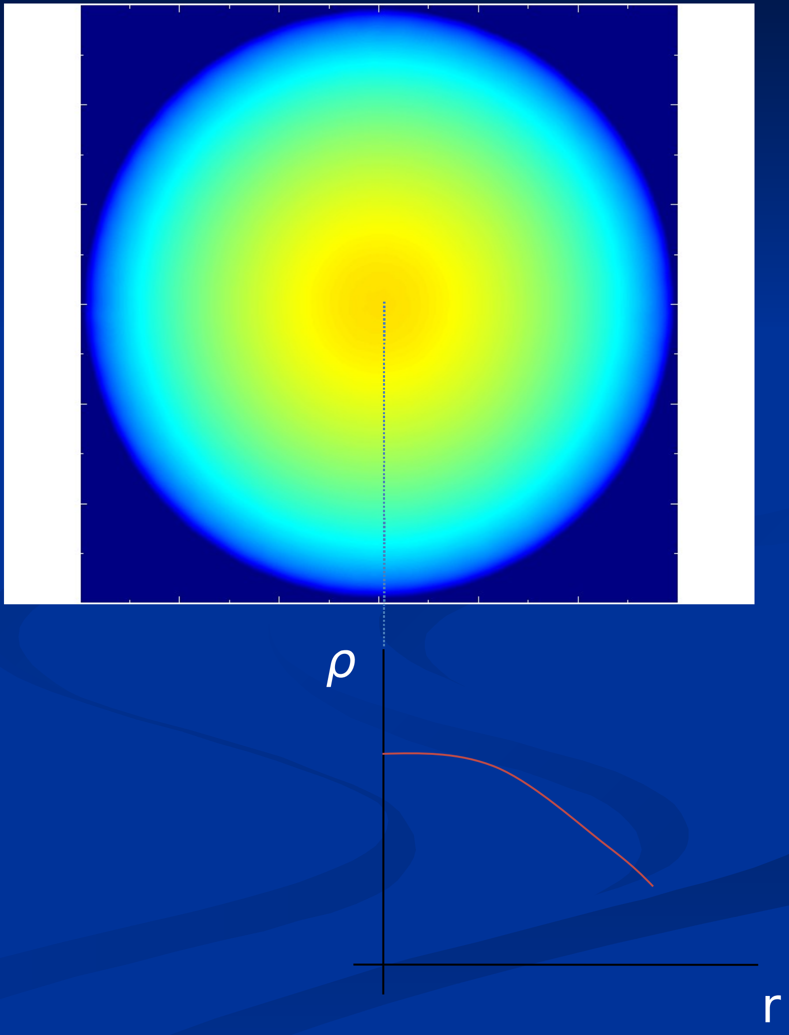

Radiation Driven Compression

Lefloch & Lazareff test

Bisbas et al. (2009)

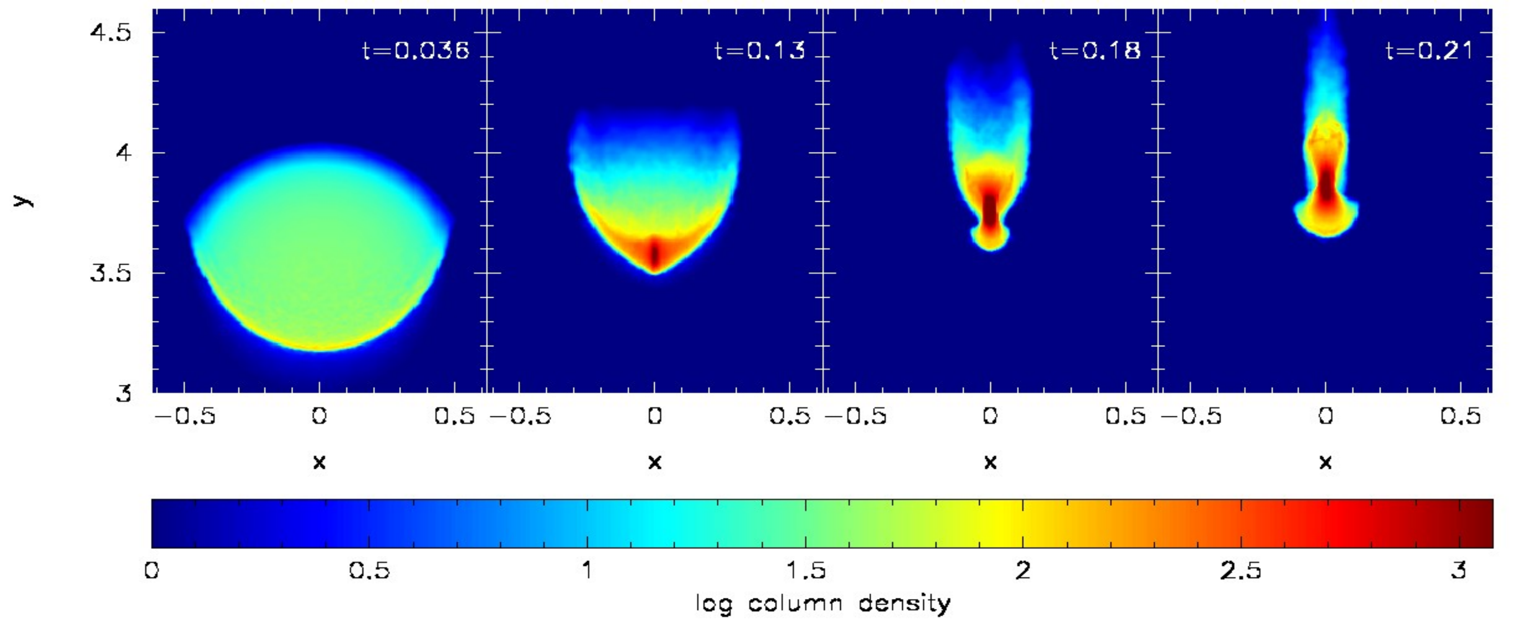

Lefloch & Lazareff (1994)

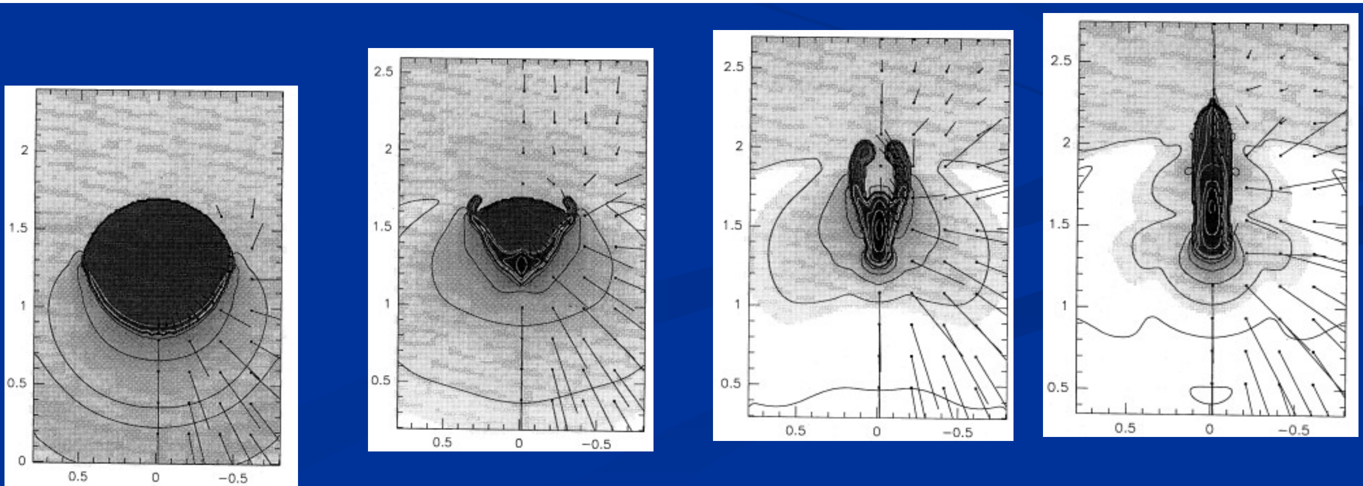

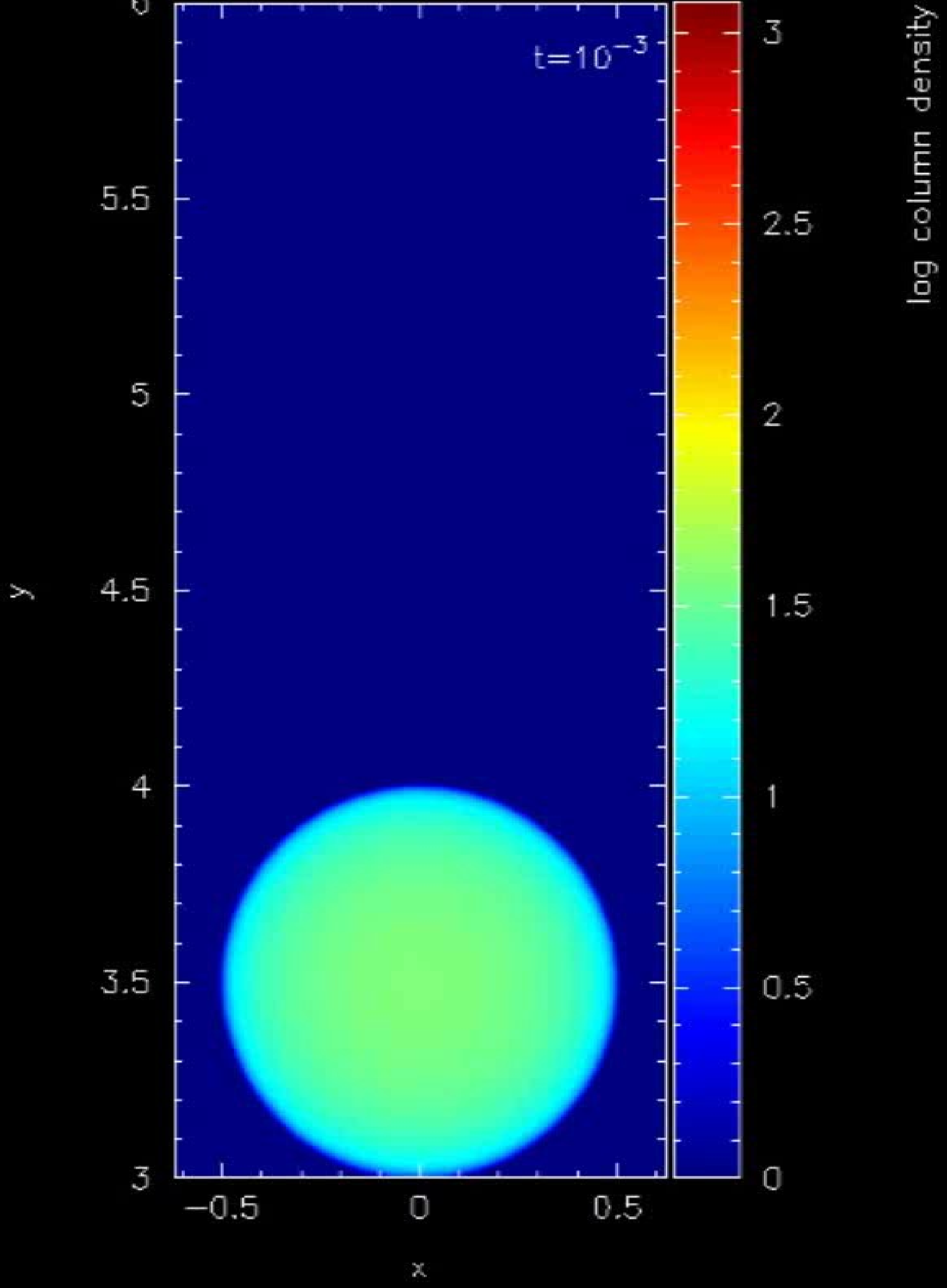
t=10^-3
y
6
5.5
5
4.5
4
3.5
3
x
−0.5
0
0.5
log column density
3
2.5
2
1.5
1
0.5
0

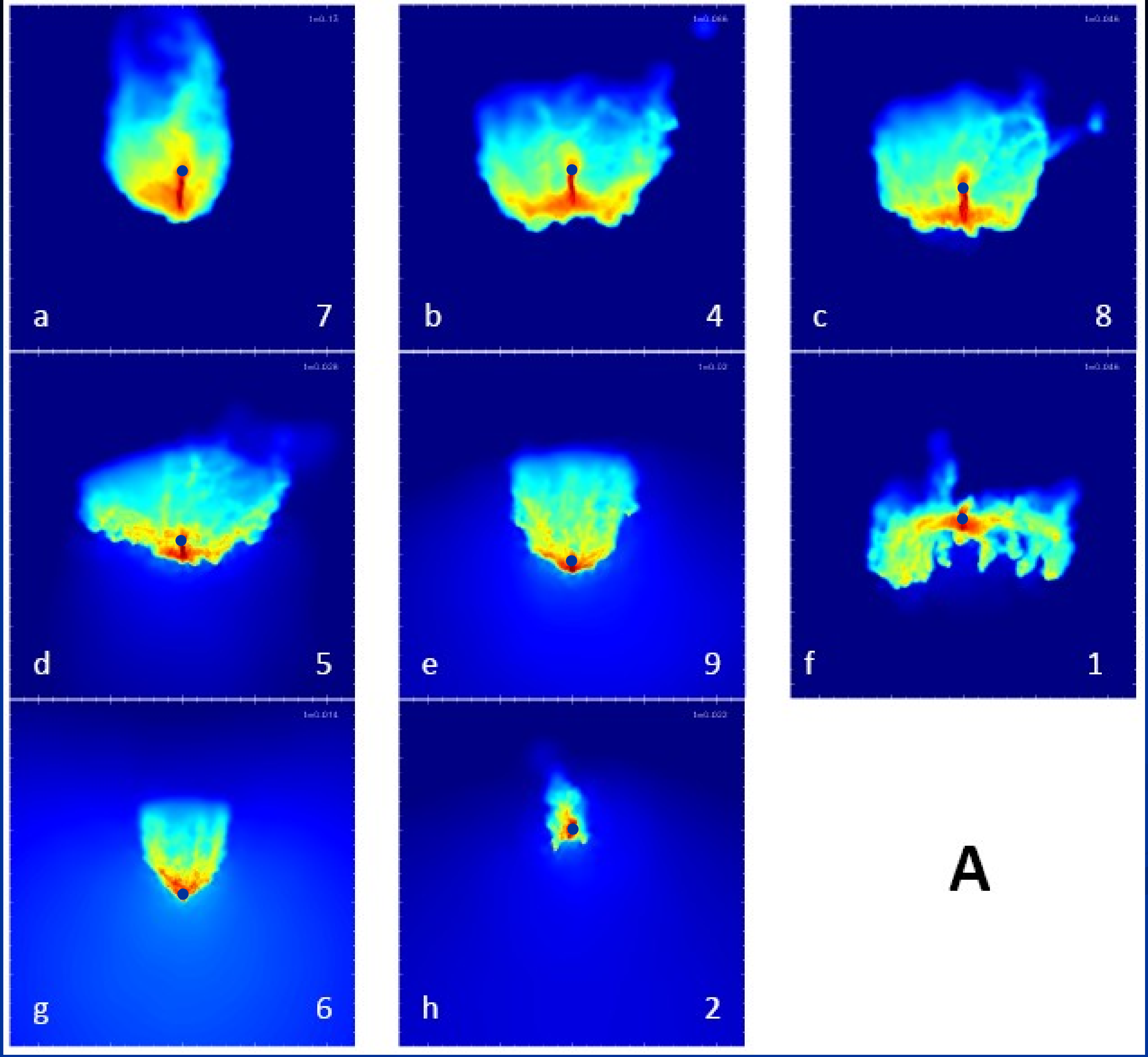
a
7
b
4
c
8
d
5
e
9
f
1
g
6
h
2
A

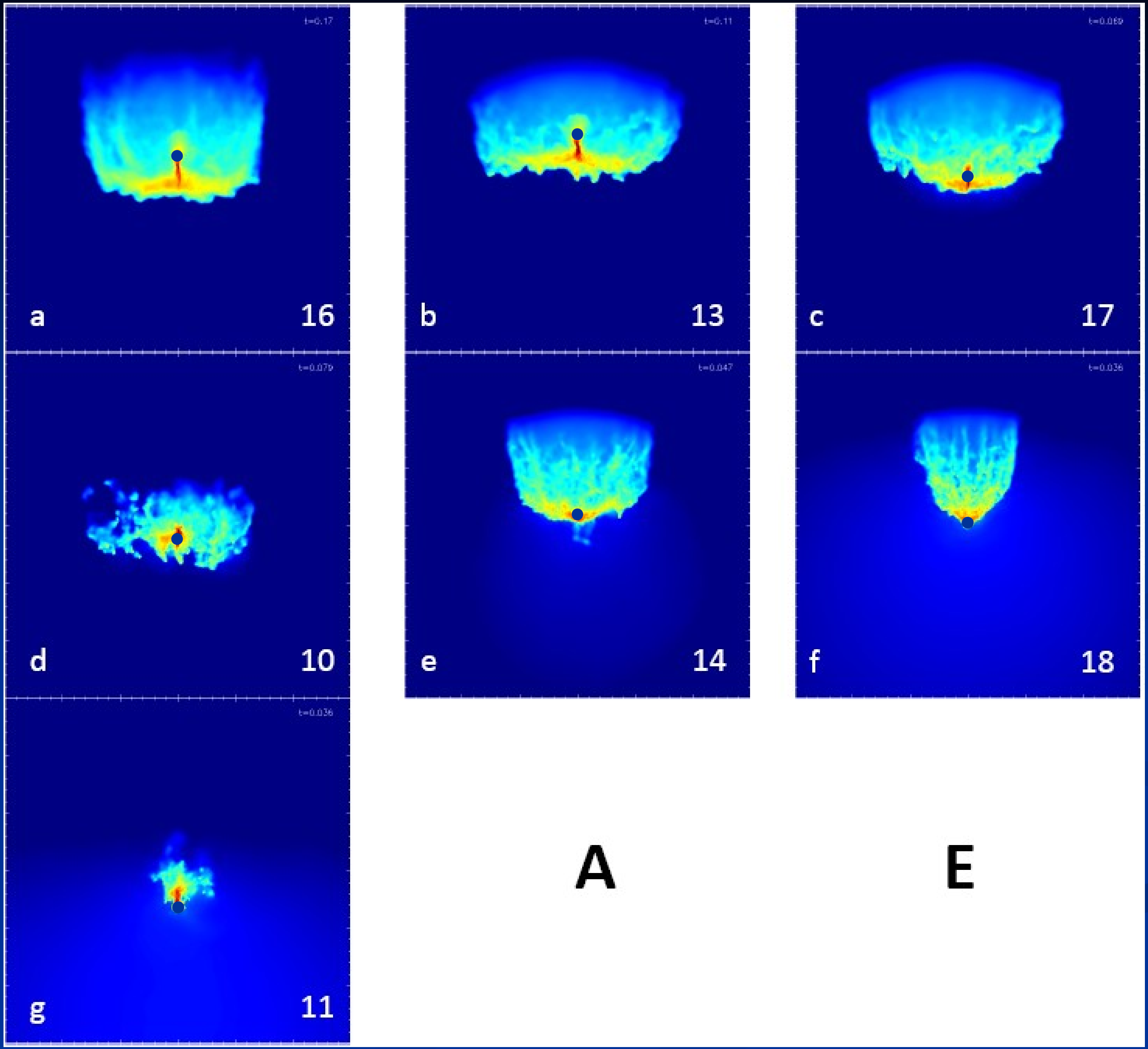t=0.17
a
16
t=0.11
b
13
t=0.069
c
17
t=0.079
d
10
t=0.047
e
14
t=0.036
f
18
t=0.036
g
11
A
E

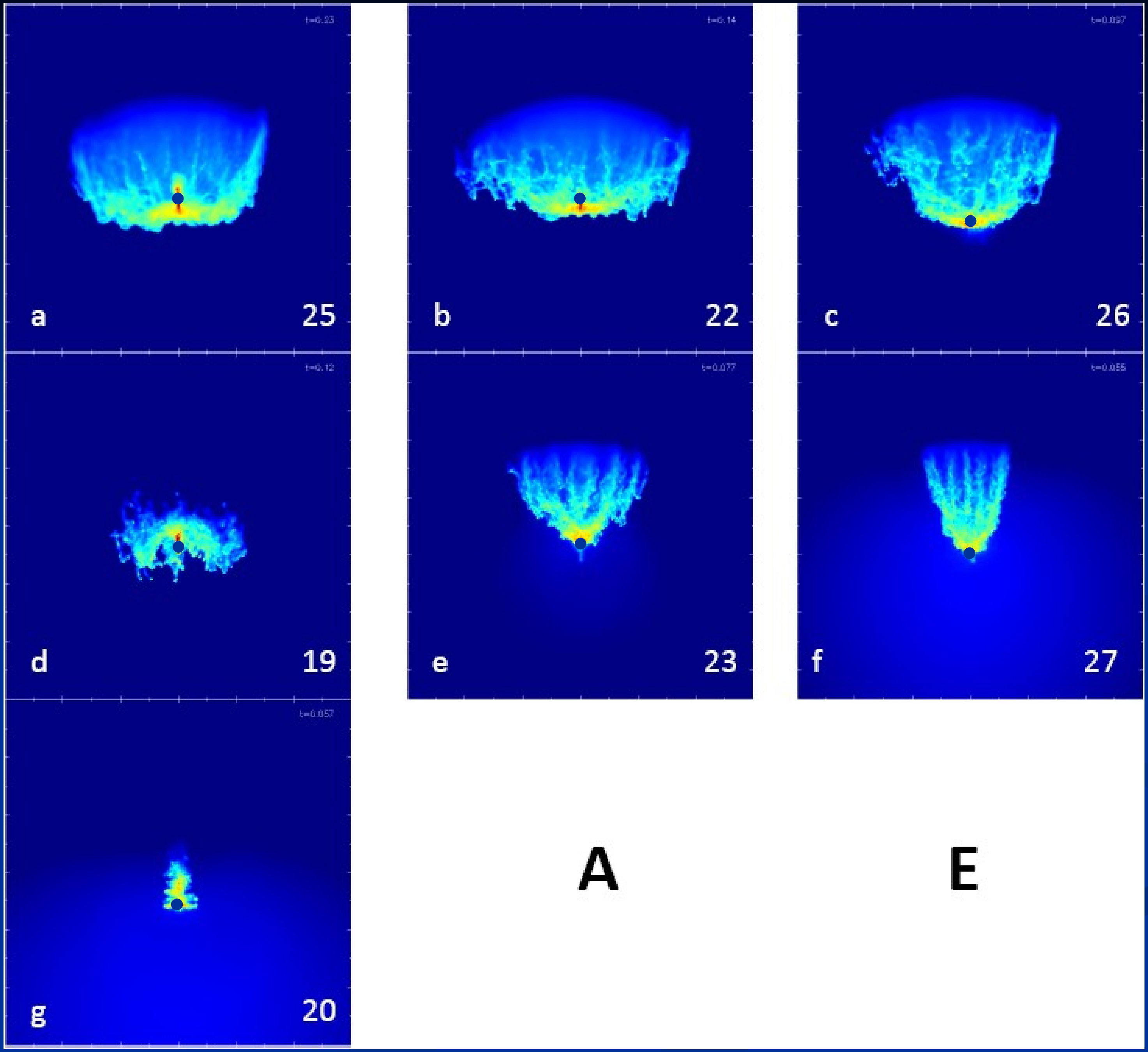
t=0.23
a
25
t=0.14
b
22
t=0.097
c
26
t=0.12
d
19
t=0.077
e
23
t=0.055
f
27
t=0.057
g
20
A
E